The Telescope Array Project

Makoto Sasaki
on behalf of the Telescope Array collaboration

Institute for Cosmic Ray Research, University of Tokyo, Kashiwa 277-8582
sasakim@icrr.u-tokyo.ac.jp

(Received)

Eight cosmic ray air shower events have been reported by the AGASA group with energy in excess of 10^{20} eV. Space becomes opaque to particles with energies in excess of several times 10^{19} eV because of the 2.7 K cosmic microwave background. The sources for these extremely high energy particles need to be less than about 50 Mpc from the earth. Particles with energies in this range are expected to be deflected very little by magnetic fields within or beyond the galaxy. Yet none of these high energy cosmic rays points back to a possible known source. In order to clarify this scientific mystery, the hypotheses concerning cosmology, elementary particle theory, and astrophysics, like cosmic string, magnetic monopole, secondary particles decayed from long-lived super heavy particles, and the breaking of the special relativity. The Telescope Array project will observe extremely high energy cosmic rays and neutrinos with the reflective mirror telescope system which detects air fluorescence yielded by air showers fallen in several tens thousands km^2. The Telescope Array detector will measure the energies, arrival directions, and particle identities so precisely that it aims at the elucidation of the extremely high energy cosmic ray origin.

KEYWORDS: Telescope Array, AGASA, cosmic ray, particle astrophysics, highest energy, extremely high energy, GZK mechanism, Super-GZK puzzle, air fluorescence, neutrino astronomy, topological defect, cosmic string, active galactic nuclei, gamma ray burst

§1. Introduction

Akeno Giant Air Shower Array (AGASA) is currently the world largest air-shower array which covers a detection area of approximately 100 km^2 with 111 plastic scintillation counters. The AGASA group has published its results on the discovery of 8 air-shower events with the primary energies beyond 10^{20} eV from recent 9 years observation [1] (Fig. 1). The unambiguous discovery of cosmic rays above 10^{20} eV is of exceptional astrophysics interest as judged by the recent flood of theoretical papers. Fly's Eye in U.S. and Yakutsk in Russia have also observed one event with similar energy respectively.[2)3)] These primary energies are more than seven orders of magnitude higher than can be achieved by the most powerful man-made accelerator and four or five orders of magnitude lower than that unified energy scale predicted by Grand Unification theory.

These highest energy particles raise scientific mysteries. Shock acceleration in galactic supernovae can account for energies to about 10^{15} eV. Violent activity in astrophysics objects such as powerful radio sources and active galactic nuclei (AGN) can account for much higher energies. No mechanism, however, has been identified that will give rise to the highest cosmic rays observed. Among possible candidates, there are none within 100 Mpc of the earth.

Another mystery is that space becomes opaque to particles with energies in excess of 5×10^{19} eV because of the 2.7 K cosmic microwave background. Greisen and Zatsepin and Kuzmin independently pointed out that this

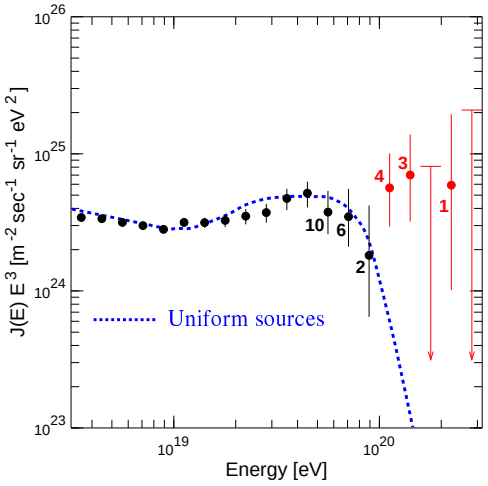

Fig. 1. The published spectrum of extremely high energy cosmic rays observed by AGASA. Vertical axises stands for measured flux multiplied by E^3.

radiation would make space opaque to cosmic rays of very high energy (GZK mechanism).[4)6)] This limitation implies that the sources for these highest energy particles need to be less than about 50 Mpc from the earth. Understanding the origin of energetic charged particles depends on a knowledge of magnetic fields through which they travel. Assuming the fields were uniform and the

order of 2-3 μG within or near the galaxy, light nuclei are hardly contained by the galaxy while protons of this energy must have extra galactic origins. Given our understanding of fields within the galaxy and intergalactic space cosmic ray protons near 10^{20} eV will suffer only a few degrees deflection from nearby sources. None of these high energy cosmic rays, however, points back to a possible source yet.

There are more exotic possibilities for sources. A curious coincidence between the energy flow of the highest energy cosmic rays and gamma ray bursts (GRB) suggests a possible common source.[7] Another speculation is that very high energy cosmic rays may be the result of annihilation of topological defects left over from the early universe.[8)?)] The energy scales of such events are of the order of 10^{24} eV (GUT scale). Beyond these ideas is the possibility that the highest energy cosmic rays are evidence for new particle physics or new astrophysics. The super-GZK events also provide motivation for determining whether the photo production mechanism actually occurs in the predicted way. Since this process is based on conventional and well-tested physics, but boosted to a very high Lorentz factor $\gamma \sim 10^{11}$, its absence would have radical implications pointing to a breakdown of special relativity.[12]

Cosmic neutrinos with energies above 10^{16} eV, so far unobserved, are also detectable with the Telescope Array detector and have great potential as probes of astrophysics and particle physics phenomena. They escape from dense regions of matter and point back to their sources, thereby providing a unique window into the most violent events in the universe. Whatever the sources and mechanisms by which hadrons are accelerated to extremely high energies in the source, and whatever the details of the composition (i.e. pp and/or $p\gamma \to \pi^{\pm}$) and subsequent decay of accompanying pions is expected to result in neutrino fluxes through the decay process: $\pi \to \mu + \nu_{mu} \to e + \nu_e \nu_\mu + \nu_\mu$, leading to the familiar ratio ν_μ/ν_e=2. Observations of cosmic rays with energies beyond the GZK cutoff also raise strong interest in extremely high energy neutrinos. All of new proposals for exotic sources inspired by the super-GZK events can lead to neutrino fluxes well above those guaranteed by the GZK mechanism.

The neutrino fluxes of some representative sources are given in Fig.2. The detection of extremely high energy cosmic neutrinos, however, very difficult especially for those with energies above 10^{17} eV. At these energies, the neutrino interaction length is below 2000 km water equivalent in rock, and so upward-going neutrinos are typically blocked by the Earth. This shadowing severely restricts rates in underground detectors such as AMANDA/IceCube, which, although sensitive to such high energy neutrinos,[13] are bounded by detection volumes of at most 1 km^3. At the same time, the atmosphere, with vertical depth 1000 g/cm^2, is nearly transparent to these neutrinos. The next generation cosmic ray detectors like Pierre Auger Observatory and Telescope Array, however, can have target volumes of atmosphere, which are so competitive with or more than that of IceCube that annual detection rate assuming AGN-jet proton acceleration models are statistically sizable.[14)15)] Telescope Array using air fluorescence technique is advanced for primary neutrino identification discriminating from proton induced air showers. Recently a novel detection strategy for earth-skimming extremely high energy neutrinos has been quantitatively proposed that improvements of two orders of magnitude are possible at the Telescope Array detector comparing to that for downgoing neutrino detection.[16] Encouragingly, extremely high energy cosmic neutrino sources except for AGN-jets like Greisen photo production ,[17] topological defects ,[19] long-lived super heavy particles, and Z-bursts [20] may be experimentally tested well with Telescope Array.

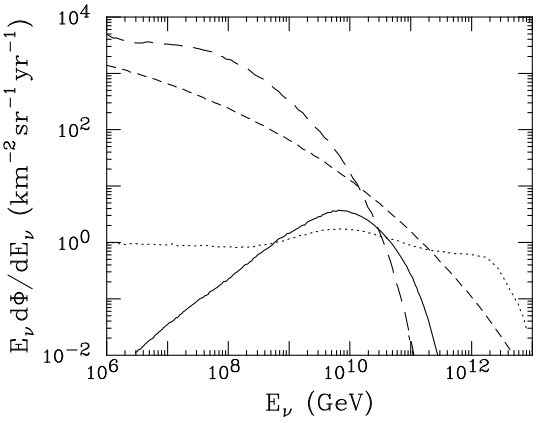

Fig. 2. Differential fluxes of muon neutrinos ($\nu_\mu + \bar{\nu}_\mu$) from Greisen photo production [17](solid), active galactic nuclei [18](long dashed), topological defects [19](short dashed), and Z-bursts [20](dotted).

§2. Telescope Array

2.1 Project

The Telescope Array (TA) detector (Fig.3 and 4) has been designed in order to clarify the mystery of the origin of the highest energy cosmic rays.[21)22)] For this purpose, the detector is required to obtain much more statistics of events than AGASA has done at the rate of one super-GZK event per year. Also it should provide particle identification as well as accurate directional determination of the primary cosmic ray to test the source models at a high confidence level. The basic concept guiding the design is to detect the image of fluorescence light yielded in air showers in a huge effective aperture, from which the longitudinal shower development is reconstructed.

The air fluorescence technique has a great advantage to discriminate photon and neutrino from other primary cosmic rays respectively. The photon identification can be a sword to distinguish between particle physics origin and astronomical one as a super-GZK source, as described later. The high energy neutrino detection is a direct evidence of the hadron accelerator model, which is one of solutions for the GZK-puzzle. To detect statistically enough number of neutrinos from AGN overcoming

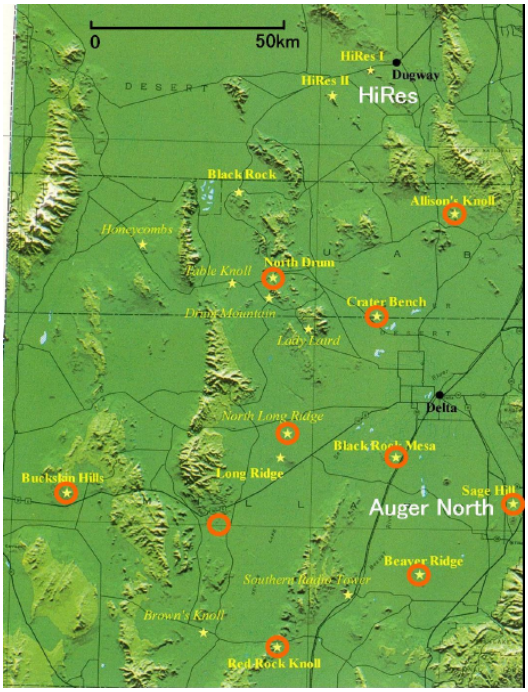

Fig. 3. TA site arrangement.

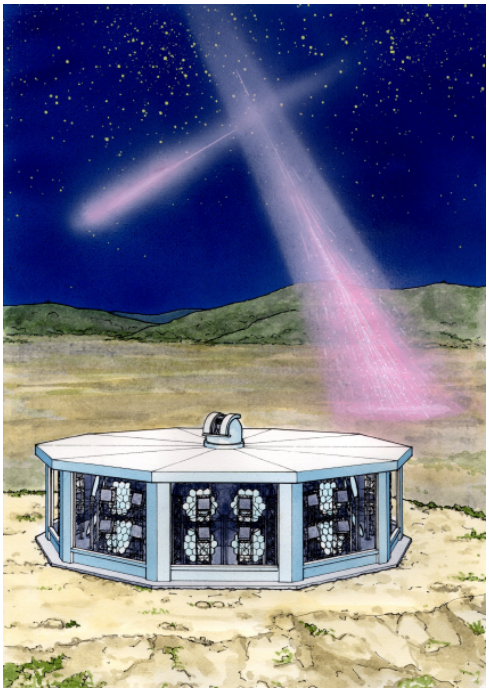

Fig. 4. TA detector station.

low interaction rate in the air, the lower energy threshold is demanded to be as low as possible. Also, to know the primary component of cosmic rays in the wide energy range between knee and the highest energy regions is very useful to completely eliminate the possibility of heavy elements in our galaxy as a candidate.

The TA detector consists of 10 observational stations installed on the line in about 30-40km interval as shown in Fig. 3. Each station consists of 40 telescopes with 3m-diameter f/1 mirror system on 2 layers of supports. 256 2-in PMTs mounted on the focal plane are served as pixels of the fluorescence sensor of each telescope. Each PMT covers the visual field which makes $1.1^\circ \times 1.0^\circ$ to be angular aperture. We expect detection rate by the TA detector for the events with the energy exceeding the GZK-cutoff is more abounding than that of AGASA about 60 times. Accuracy of determining of the energy and arrival direction for the highest energy event are roughly 20 % and 0.5 deg respectively. The detailed simulation study is described later.

To keep good visibility, atmospheric transparency, no significant nearby sources of light pollution, and away from main traffic, the detector stations are preferable to install on top of small mountains or hills without sacrificing arrangement in 30-40km interval. We have selected sites in southern part of Utah state, south-west area of Delta. The present ten candidates of the locations where the TA stations will be installed are: Allison's Knoll, North Drum, Crater Bench, south of Long Ridge, North Long Ridge, Buckskin Hills, Sage Hill, Black Rock Messa, Beaver Ridge, and Red Rock Knoll. The detector station array is expanded in 200km square area.

We have already submitted the request for the construction budget of \$60 M to our funding agency; Ministry of Education, Culture, Sports, Science and Technology, which pays the 4-year construction of the detector before the full operation of the observation from 2006.

2.2 Air Fluorescence

The highest energy cosmic rays can only be observed on the earth by way of their interaction in the earth's atmosphere. Cascades of particles are initiated by cosmic ray particles striking air molecules. The shower cascade peaks at a depth of about 800 g/cm^2 in the atmosphere. The shower arrives at the earth's surface as millions of particles. Gammas (∼89%) and electrons (∼10%) of about 10 MeV dominate. There are also muons (∼1%) with energies of about 1 GeV.

The two most commonly used methods for air shower measurements are those detecting atmospheric fluorescence and those measuring particle densities on the surface. On dark moon-less nights, nitrogen fluorescence produced by air shower induced ionization can be detected by a sky covering array of photomultipliers, which has a 10% duty cycle as compared to the surface array. This method was pioneered by the Fly's Eye group at the University of Utah. The compound eye type detector observes the shower as a spot of light moving across the sky. By measuring the amount of light and timing of the photons, the compound eye can directly measure the energy deposition profile.

Of the two air shower detection methods, fluorescence detection provides a more direct measure of the energy and particle identification. The light due to ionization is a measure of the electromagnetic shower size and hence the energy. The measurement of the longitudinal devel-

opment of the electromagnetic shower provides the interaction length of the primary particle which induces the air shower in a statistical way.

Once the track geometry is known, the PMT signals are sliced into some angular along the track. Various attenuation effects between source and detector such as ozone absorption, aerosol and Rayleigh scattering are taken into account. It should be enhanced that the observation of air shower with air fluorescence method is fully based on total-absorption calorimetry using atmosphere as an active target and as an absober. The reconstruction in the air fluorescence method is described later.

Surface array detectors, on the other hand, depend on comparison to simulated showers. Although the earliest interactions of the simulated showers depend on particle production models that extrapolate from accelerator data, the particle densities on the ground are rather insensitive to these processes. This method suffers a lack of information of longitudinal development but it can utilize only the 2D-measurement of position and timing.

2.3 Light Collector

We have employed a spherical mirror optics to obtain a wide field of view (FOV) with reasonable focusing power, with which support and adjustment mechanism for segmented mirror is simpler than that with the parabolic one.

The telescope has a main dish with a diameter of 3.3 m which is composed of 18 hexagonal shape segment mirrors (see Fig.7). The attachment angle of each mirror is adjustable in two directions. The location of the central mirror is made empty and is reserved for the optical alignment system and PMT calibration system. The detailed design parameters of the telescope and the segment mirror is given in Table I.

Table I. Design parameters of TA telescope.

Telescope	
Diameter	3.3 m
Total Mirror Area	6.8 m^2
Focal Length	2960 mm
Mirror Optics	spherical
FOV	18° horiz. × 15.5° vert.
Wind Velocity for Operation	$\leq$ 15 m/sec
Number of Segmented Mirrors	18
Segment Mirror	
Shape and Dimension	hexagonal, 660 mm between opposing edges
Mirror Area	0.377 m^2
Radius of Curvature	6067 ± 40mm
Spot Size	$\leq$ 10mm FWHM
Base Material	Tempax glass, 10.5 mm thick
Mirror Coating	aluminum
Surface Protection	anodization; Al_2O_3, $\sim$ 50 nm
Reflectivity	$\geq$ 88 % at 350 nm
Weight	10.7 kg

A ray tracing simulation is made for the spherical mirror telescope with a planar imaging plane located near the focal point. The result is shown in Fig. 6. Parallel light beam was injected every 4° in horizontal and vertical directions and its image on the camera is plotted. The obscuration by the PMT camera is taken into account. The spot size of 30 mm in FWHM is obtained in most of the FOV. It is sufficiently small compared with the PMT dimension (61 mm between two opposite edges of hexagon) and does not contribute much for determining the resolution of the telescope. The mirror

Fig. 5. The prototype telescope unit.

is made by 10.5 mm thick Tempax glass (Schott corp.). A support disk of 150 mm diameter made by the same material is glued behind the mirror by 3M Dymax 840 glue. The disk is used to support the segment mirror from the telescope frame.

The segment mirror is shaped by heating a planar glass on a ceramic mold plate in the temperature controlled electric oven. Including the annealing, the production process takes one day to make one mirror. We expect the specification of the mirror is achieved without significant polishing. The mirror surface is coated with 200 nm thick aluminum produced by the vacuum deposition. A hard protection surface of Al_2O_3 crystal with thickness of 50 nm is then produced in the solution containing ammonium hydroxide, tartaric acid and ethylene glycol. The reflectivity greater than 88% is obtained between 330 nm and 450 nm. This curve can be adjusted to have a peak around 350 nm by tuning the thickness of anodization. The anodized surface is stable and the degradation of the reflectivity is $\sim$ 1 %/year from the experience of the Fly's Eye group. The mirror surface can be washed by pure water for the regular maintenance in the field.

We are simulating the distortion of the mirror system

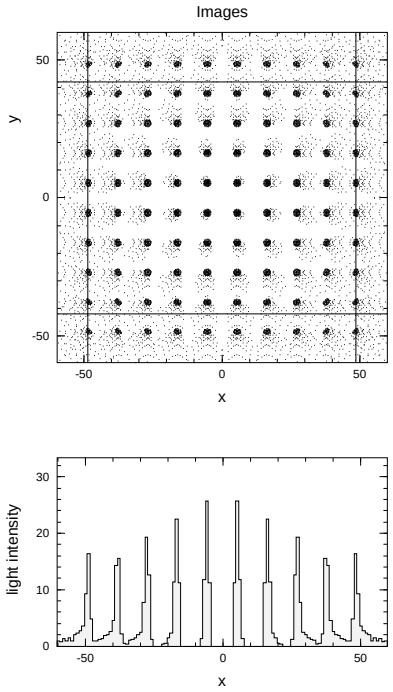

Fig. 6. Expected image of TA telescope unit.

Fig. 7. The prototype camera unit.

Table II. Characteristics of the Hamamatsu R6234

Shape and Dimension	hexagonal, 60 mm diagonal
Dynode Structure	box-line focus
Number of Dynodes	8
Quantum Efficiency (max.)	30 %
Gain (typ.)	2.7×10^5 (1000 V)
Anode Dark Current (typ.)	2 nA
Anode Dark Current (max.)	20 nA
Rise Time	6.0 ns
Transit Time	52 ns

by the high velocity wind using the finite element analysis. The displacement of the mirror is to be less than a few mm under the wind velocity of 15 m/sec. Such a high speed wind occurs in less than 1 % of the observation time according to the weather monitoring at Dugway Proving Ground, where Fly's Eye and Utah Seven telescope groups had been operated. The temperature coefficient of the focal length was measured and found to be negligibly small (0.3 mm/degree).

Safety hazard tests were made for the prototype mirrors by destroying the mirror by applying the impulsive shock at the edge of the mirror. The present design stands for the shock applied with a momentum of 250 kg m/sec, which corresponds to a kick or a straight punch to the mirror by human adults.

2.4 Imaging Device

A set of 256 hexagonal PMTs is arranged in 16×16 array to form an imaging plane of the camera. A single camera covers the sky of 18° in azimuth and 15.6° in elevation with a pixel acceptance of 1.1° × 1.0° for one PMT. A UV transparent filter (BG3) with a thickness of 6 mm is placed in front of the PMT to reduce the number of night sky background photons.

The PMT planned to be used in the Telescope Array project is Hamamatsu R6234, which has a hexagonal bialkali photocathode and borosilicate glass window. The PMT has 8 dynodes of a box-line focus type and a typical gain of 2.7×10^5 at 1000V. Characteristics of the PMT are summarized in Table II. The night sky background is approximately 30 photoelectrons in 200 ns and it is equivalent to the anode current of 1.9μA at the gain of 8×10^4 (see §2.6 for details). This is not completely negligible compared with the maximum bleeder current of ∼ 0.2 mA. Moreover, the anode current fluctuates continuously during the observations. This fluctuation changes the PMT gain significantly when we use an ordinary bleeder circuit by the register chain. In order to avoid this problem, we developed a hybrid bleeder circuit using Zener diodes at the last 2 stages of the dynode chain (see Fig. 8). The measured variation of the pulse

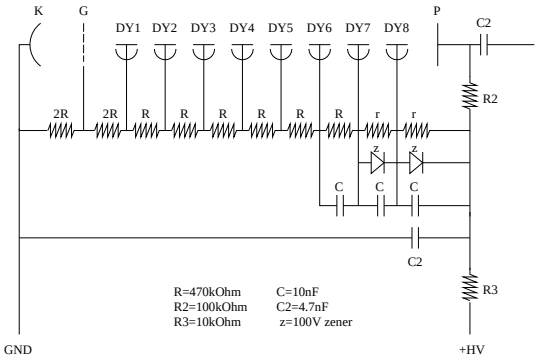

Fig. 8. Hybrid bleeder circuit with Zener diodes.

gain against the background anode current is shown in Fig. 9. As shown in the figure, the pulse gain of the hybrid bleeder is almost constant in the wide range of anode currents.

Following the simulation, the largest PMT signal to be detected is 6×10^4 photoelectrons in 200 ns time window (see §2.6 for detail). This corresponds to 4.2 mA anode current assuming the PMT gain of 8×10^4. The linearity of PMT depends on the relative voltages applied to the last few dynodes. In Fig. 10 we show the linearity measured for the various types of bleeder circuit. The hybrid bleeder with Zener diode shown in Fig. 8 (filled circle) gives the optimum result. The deviation from the linear response is ~ 1 % for the anode current of 4.2 mA, and is within 5 % up to 20 mA, which is sufficient for the TA's requirement.

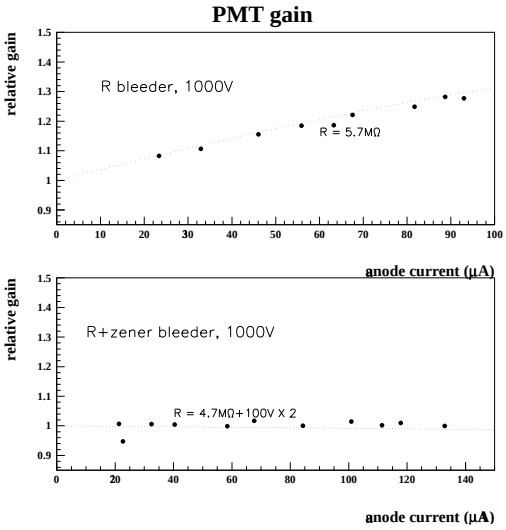

Fig. 9. Pulse gain variation against background anode current, with the ordinary bleeder circuit (a) and with the hybrid bleeder circuit (b).

The PMT camera is exposed to the ambient air during the observation. The gain of PMT may vary from hour to hour reflecting the temperature change of the PMT and bleeder circuit. It is necessary to measure the temperature dependence of the PMT pulse gain and correct its effect in the data analysis. We measured the PMT gain variation for the ordinary and the hybrid bleeder circuit for a temperature range from -20°C to 40°C. The results with the ordinary bleeder is shown in Fig. **??** (a). The temperature coefficient is -0.39 ± 0.02 %/K and it is consistent with the typical temperature coefficient of $-0.2 \sim -0.5$ %/K for the bialkali PMT. The result of the same PMT with the hybrid bleeder is shown in Fig. **??** (b), and the coefficient is -0.57 ± 0.03 %/K. This result is larger by 0.2 %/K than that of the ordinary bleeder, which can be explained by the temperature coefficient of Zener diodes (0.095 %/K in typical).

We plan to use the optical filter, Schott BG3, passing photons only from 300 to 400 nm wave length. Since the transmittance of the filter depends on the thickness, we estimated its best thickness by referring to a signal to noise ratio (S/N). The S/N increases with the filter thickness, but is almost constant for the thickness more than 6 mm. We have chosen the filter thickness of 6 mm.

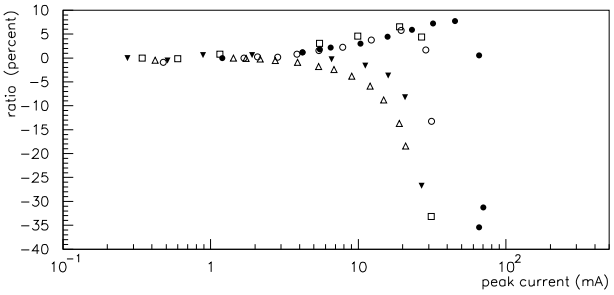

Fig. 10. Measured linearity of the pulse gain for various bleeder circuits. All the measurements are made under the conditions of same pulse gain $\sim 10^5$ (i.e., HV values are different). The light pulse width is 300ns. All the bleeders have the same registers until DY6, as same as shown in Fig. 8. The resistances of (DY6–DY7),(DY7–DY8) and (DY8–P) are; *open circle*: R,2R,1.5R, *open triangle*: 2R,2R,2R. And the voltages of Zener diodes of (DY6–DY7),(DY7–DY8) and (DY8–P) are; *filled triangle*: 75V,130V,95V, *open square*: 62V,130V,100V, *filled circle*: R,100V,100V.

The sensitivity of the PMT has a position dependence on its photocathode surface, reflecting the non-uniformity of the quantum efficiency and the amplification gain. Various factors such as the photocathode thickness, the irregularity of the focusing electric fields and the geometry of the first few dynodes affects the position dependence. We measured the 2-dimensional response of the PMT by scanning the pulsed LED source on the PMT window. The light source was mounted on a computer controlled XY stage. The spot size, as well as its relative positioning accuracy, was $\sim$ 1mm. The measured anode gain map is shown in Fig. 11.

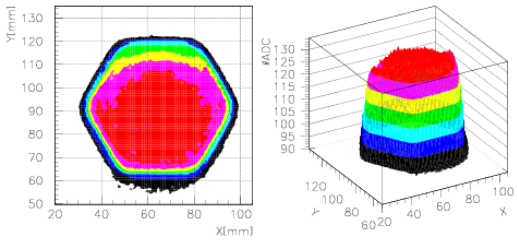

Fig. 11. Contour map of the measured anode gain (relative).

As we observe from the sensitivity map, there is $\sim$ 3 mm insensitive region at the edge of the PMT glass envelope. Together with the physical gap between PMTs, it will form an insensitive band of 7–8 mm at the boundary of the PMTs. We are in the process of estimating the loss of fluorescence light and the effect on the event reconstruction by the simulation. At the same time, we are designing a wedge-shaped reflector to be placed at the PMT boundary such that the fluorescence light im-

Table III. Power consumption in a PMT camera box. The values are measured for the prototype circuits.

parts	power	
CSI-hybrid	1.75	W/ch
ADC+DSP	0.75	W/ch
Main	5	W/16ch
Front-end circuit	720	W/256ch
HV distributor	120	W/256ch

pinging on the insensitive band is reflected and guided to the central region of the photocathode. This minimizes the insensitive area and improves the uniformity of the imaging plane, thus minimizing the systematic error.

The PMT camera is to be made as a closed box to avoid the PMT and electronics be damages by the sand and dust of the environment. In addition, the ambient temperature varies from -10 to $40°$C, and the electronics inside the camera box is a heat source of 1.7 kW (estimated with a safety factor of 2, see Table III for detail). To cope with this problem and guarantee a stable operation of the camera, it is imperative to equip the temperature control system inside the camera box.

In the overall design of the PMT camera, each PMT is inserted to an accurately machined hole of the aluminum support plate and fixed with 4 screws. The front of the camera is covered with an optical filter, Schott BG3, attached to the frame, which can be opened for the access to the PMT for the maintenance. A computer controlled XY scanning stage is attached to the filter frame carrying the YAP pulser for the calibration of PMT and electronics. The back of the PMT is covered by two doors, to which VME crates for the main digitizer/trigger board and HV distributors are installed. The inner wall of the box is covered with heat insulators. A small air conditioning unit is installed inside the box for cooling the electronics. The outer dimension of the box is 1300 mm $\times$ 1150 mm $\times$ 905 mm and the total weight of the camera including the PMTs and the electronics circuits is about 250 kg. Since most of the digitizer and trigger electronics are installed inside the camera box, the number of cables coming out from the camera is much reduced, and only a few optical fiber cables and power supply cables are to be connected to the camera box.

2.5 Calibration of PMT

An online gain monitoring system of high quality is indispensable to maintain the accuracy of the energy calibration over a long period. In order to calibrate the gains of the PMTs and readout electronics, each PMT will be exposed before and after every observation run to UV photons from well-calibrated YAP ($YAlO_3 : Ce$(YAP) $+ {}^{241}Am$) light pulsar and UV LED on a motorized XY scanning stage which is equipped on the surface of the PMT array in the imaging device. The 2D-position of the stage can be controlled with an online computing software by the accuracy of 0.2 mm at the speed of 10cm/s. The two kinds of light sources mounted on one scanning stage make complementary roles.

The structure and characteristics of the YAP pulsar (produced by Radiation Instruments and New Components Ltd.) is shown in Fig. 12 (b) and described in Table IV, respectively.[23–26] Its luminous spectrum spans 300–400 nm covers nicely the spectrum of air fluorescence. The fast decay time of 28ns allows us monitoring the output data from ADC sampling every 200 ns independently. The temperature dependence of the emitted fluorescence lights has been measured to be 0.4%/K. This feature provides the possibility of online monitoring for the absolute gain of the readout channels on a real site once the absolute emission light intensity from the YAP pulsar is measured at a certain temperature.

Table IV. Characteristics of YAP pulsar

Diameter	5.0 ± 0.2mm
Thickness	1.2 ± 0.2mm
Pulse Frequency	$\sim$50Hz
Pulse Height Distribution	FWHM 5.5 %
Peak Wave Length	370 nm
Decay Time	28 ns
Temperature Dependence	0.4%/K (-20° $\sim$ 40°)
Emission Intensity	$\sim$ 8,000 photons/pulse

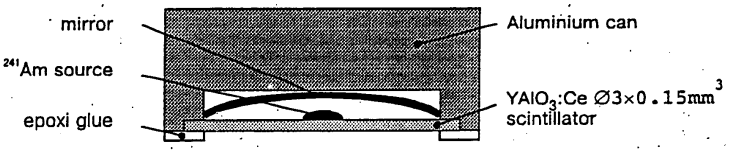

Fig. 12. Structure of YAP pulsar.

The PMT gains are adjusted by changin the applied high voltage. A prototype of the channel-by-channel high voltage supplying and monitoring system has been already developed (Fig. 13). The set value of supplied high voltage is controlled by a computer software for each PMT independently by 14bits dynamic range from 0 to 1200 V. Also the actual applied voltage for each channel can be monitored with ADC at any time. The non-linearity and temperature dependence of the set high voltages have been measured to be less than 0.6 V and 0.01 V/K respectively in the range of voltages from 0 to 1200 V. The cost of the high voltage system is expected to be roughly \$25 per channel.

The second light source is the UV LED (Nichia NSHU590E), whose characteristics are described in Table V. The main advantage is the fact that the emission intensity is controlable with the input electric current. This light source will be used to check the gain linearity as varying the input photon intensity for every readout channel before and after the observation run.

During the observation run, the time variation of the gain of each channel of the PMT and readout electronics is periodically monitored by an optical monitoring system using a xenon flash lamp. The xenon flash lamp installed in each detector station is operated at a repetition rate of 0.01 Hz by external triggers. The light

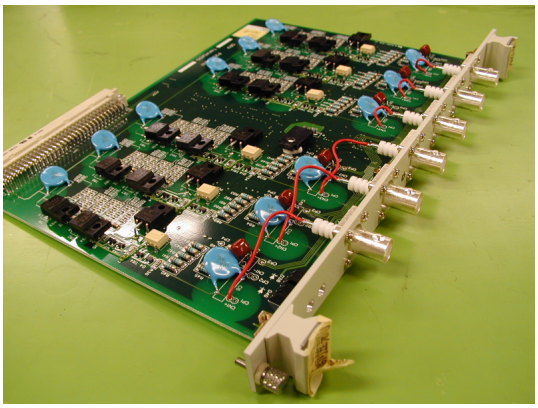

Fig. 13. Prototype of high voltage distributer.

Table V. Characteristics of UV LED (Nichia NSHU590E)

DC voltage	3.9 V
Emission Power	750μW
Peak Wave Length	370 nm
FWHM of the Spectrum	12 nm
Stabilizing Time	$\sim$2 μs
Temperature Dependence	$\sim$6%/K

output of the flash lamp is monitored by a PIN photo diode. The pulse to pulse fluctuation of the intensity observed by the PIN diode is 0.4-0.5% r.m.s. For each telescope imaging device, the xenon light is distributed through optical fiber cable connected at the center of spherical mirror dish to distribute the light uniformly on the cathode surface of the PMT.

2.6 Electronics

2.6.1 System requirement and overview

The strength and duration of the air-fluorescence pulse sensed by a PMT in the TA detector depends largely on the geometry of the event. The recording of the signal time profile becomes increasingly important for events with a long duration, for which most of the information to determine the geometry (particularly the direction) is included in the time information. Therefore the continuous digitization and recording of the signal wave form is much preferred compared to the analog integration of the signal with a fixed gate width, or a fixed time constant.

In Fig. 14, we show scatter plots of the maximum number of photoelectrons contained in 200 ns gate time v.s. its impact parameter for the 10^{21} eV proton air-shower events from Monte Carlo study. The rate of events in which at least one of the PMTs exceeded the ADC dynamic range of 12 bits (16 bits) is roughly 30% (10%) assuming a least sensitive bit (LSB) of digitization is taken equal to one photoelectron in 200 ns. The difference between 12 bits and 16 bits increases as we tighten the event selection cut. This concludes the dynamic range of 16 bits is needed for the ADC system to be unsaturated up to 10^{21} eV event. The requirement can be alleviated if we take a LSB sensitivity to be at significantly lower level, say at the level of the night sky background ($\sim$30 photoelectrons in 200 ns). But the monitoring of the background level will be unreliable for such a system, and a signal separation from the background will be much deteriorated for the online and offline analysis.

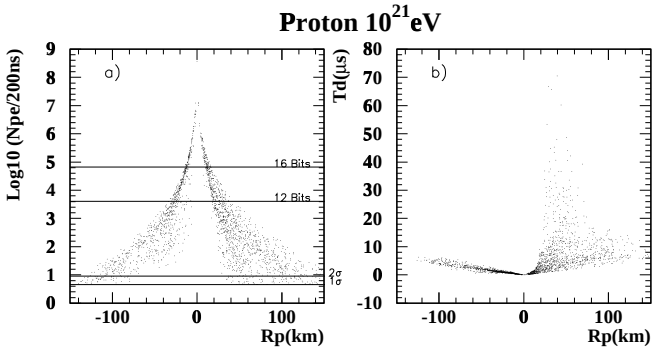

Fig. 14. Maximum number of photoelectrons per 200 ns time bin for one PMT versus impact parameter R_P of the event (left). Signal duration versus R_P for the same PMT (right). The sign of R_P distinguishes between going (plus) and coming (minus) tracks of observed air-shower events with respect to a detector station.

An elaborate and flexible algorithm will be required online and offline to identify a signal and maximize the signal to noise ratio (S/N). We checked that the 25.6 μs time window, which corresponds to 128 ADC samples and the size of one page of the internal data memory words, is practically sufficient for the signal finding for the triggering purpose (Fig. 14 b).

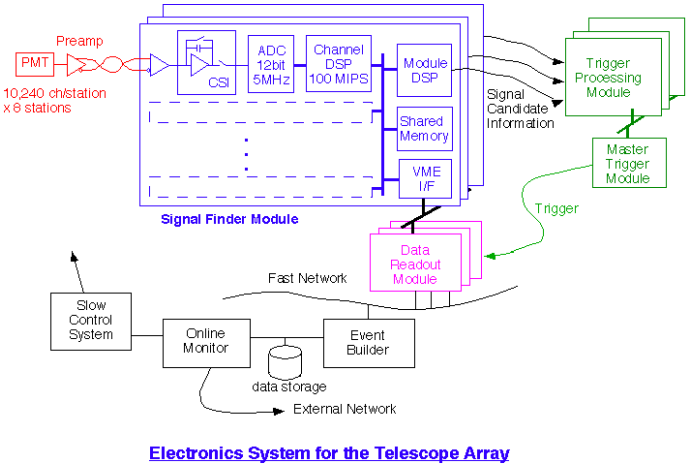

Fig. 15. Block diagram of the TA online system.

A good S/N will allow us to trigger and analyze lower energy and more distant events. As a result, we will be able to decrease the threshold energy for detection down to lower one such as 10^{16} eV, which is about an order of magnitude smaller than that of Fly's Eye. Here D is

the mirror diameter and d is the PMT diameter. This would allow us to study cosmic rays in this energy region and specifically opens up a possibility of detecting the neutrinos from a super-GZK source candidate of proton accelerator like AGN.

Monte Carlo studies indicate that many showers that trigger one station will also be seen by several neighboring stations. Even if the neighboring telescope does not see enough of the light to trigger on that shower, there will be information present useful for the stereo reconstruction of the event. The system of broadcasting triggers seen by one detector to its neighboring detectors will be thus important. When a trigger occurs in one detector, the data of its neighboring detectors will be examined and any hits found will be written into the data stream.

A design of the TA signal digitization, trigger and data acquisition (Fig. 15) has been drawn to satisfy above conditions. Its main features are summarized below:

1. AD conversion with 12-bit resolution and 5 MHz continuous sampling using a pipelined ADC chip.
2. 16-bit dynamic range using H/L 2-range scheme at the front-end charge sampling LSI (custom development). Here LSB sensitivity is taken equal to one photoelectron in 200 ns time window.
3. on-flight software recognition of fluorescence signal by the DSP attached to each channel.
4. generation of trigger in 3-dimensional space; XY (camera) coordinates and T (time) coordinate by software.
5. exchange of trigger information between stations (inter site trigger).

2.6.2 Front-end Electronics System

– Charge Integration

A charge integration method is essential in designing a calorimetric measurement. To implement the frontend electronics design, we are developing a Charge Successive Integrator (CSI) LSI. (Fig. 16). It has three rotating capacitances which serves for the integration, signal output to ADC, and reset successively for each 200 ns. Required signal range for the CSI (and PMT) is summarized in the following lists. Here we use a PMT amplification of 8×10^4, which is followed by a preamplifier circuit with the gain of 4, 100 pF storage capacitance for the CSI, and an amplification with the gain of 2 at the end of CSI. The LSB in the low range (a unity gain before CSI) corresponds to 1 photoelectron in 200 ns. The maximum signal corresponds to 65,536 ($=2^{16}$) photoelectrons in 200 ns and is detected in the high range (a gain of 1/16 before CSI).

- Least count sensitivity: A 10 ns wide (square) pulse from PMT is preamplified into a pulse with a (peak) current of 5.1 μA and a total charge of 51 fC. This is equivalent to 1.0 mV of stored voltage on the CSI capacitance (low range used).
- Full scale sensitivity: 65,536 photoelectrons in 200 ns corresponds to 17 mA current after preamplifier for the same duration. The total charge after preamplifier is 3.4 nC and this becomes 4.0 V on the CSI capacitance (high range used).
- Night sky background: We assume 30 photoelectrons in 200 ns. This is equivalent to a continuous current of 7.7 μA after preamplifier and 31 mV stored on the CSI capacitance (low range used).

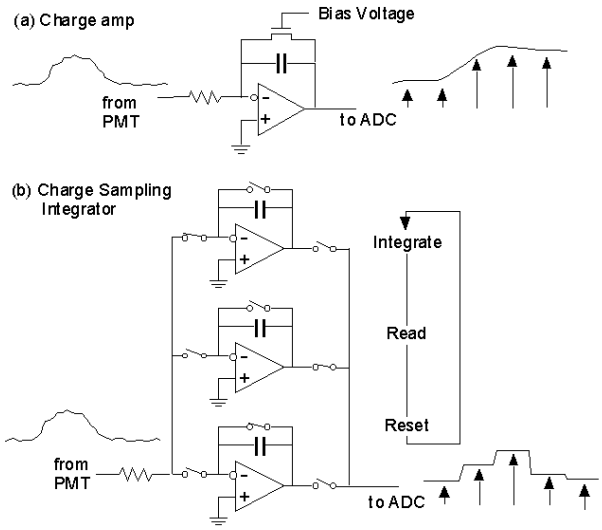

Fig. 16. Schematics of Charge Successive Integrator.

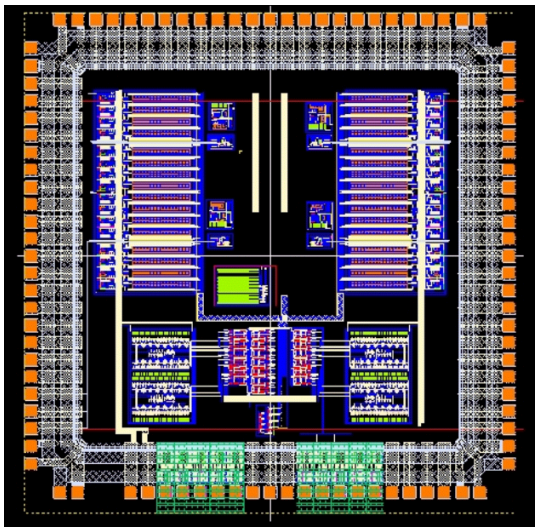

Fig. 17. Layout of the test CSI cell designed in 0.6 μm CMOS technology.

The CSI will be fabricated in a CMOS technology. In this technology the value of the capacitor matches in 0.1% level, and no correction will be necessary. But the area of CSI-VLSI limits the integration capacitance less than ~200 pF. A test CSI chip using a 0.6 μm single-poly, triple-metal CMOS process was fabricated (Fig. 17) at Rohm Co. through VLSI Design and Education Center (VDEC, Univ. of Tokyo) multi project ware service. The prototype CSI chip includes four sets of two range of

circuits.

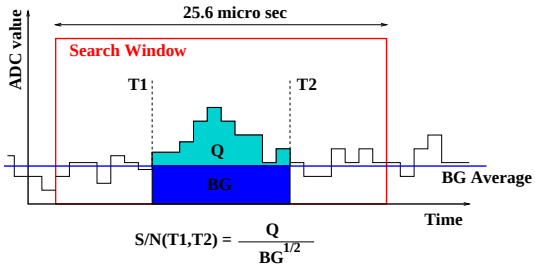

Fig. 18. Signal finding algorithm.

– *Pipelined ADC*

In the pioneering work of the Fly's Eye detector, analog sample-and-hold circuit with a slow AD converter[27] was adopted. In the subsequent HiRes detector, 8-bit flash ADC was introduced with additional analog sum measurements to circumvent the effect of over range.[28] While the fast ADC system could give us more information on air shower, it increases data size almost 100 times. Thus a large bandwidth is required in data acquisition system. Furthermore, to maximize the merit of the fast digitization, it is indispensable to process the data in real time to increase signal to noise ratio. This is particularly important in the fluorescence measurement since the signal wave form varies greatly depending on the zenith angle and the impact parameter.

Recent progress in digital video system brings a new high-speed, large dynamic-range, low-power, low-cost ADC. Technique used here is called pipelined ADC. The ADC has many pipelined stages, and digitization of only one or two bit is done at each stage. This ADC is fabricated in similar process used in CMOS digital LSIs and there are very little analog elements in the chip. A digital error correction technique is usually employed to achieve a high precision. We are presently using Burr-Brown ADS803 and its power consumption is only 115 mW. The ADC has 12-bit dynamic range and 5 MHz-conversion rate.

– *DSP*

To process the digital data in real time, a large processing power is required. Fortunately, recent progress in digital products introduces high-performance, low-cost DSPs. There are several DSPs, performances of which are more than 100 MIPS and the price is about $6. By using these DSPs we will be able to search optimal signal width for fluorescence signal in real time. The ADC converts a PMT signal continuously at 5 MHz frequency, and 12-bit data together with additional information such as a range and an overflow bit are successively stored into the memory of dedicated DSP. A high-performance DSP is needed to run a signal finding algorithm in real time on the stored data. We are presently using a TMS320C549 DSP from Texas Instruments. This DSP runs at 100 MHz, and many operations can be performed in one cycle. The C549 has 3 internal data bus and one program bus, and consists of 6 stage pipelines. It contains 32k word internal memory that is enough for our application. The DSP consumes only 100 mW/chip. Since the ADC generates 12-bit data every 200 ns, there are 20 cycles for one data in average. We set 25.6 μs time window for finding a signal. Since this window has 8.5 μs overlap with the next window, a total of ~1,700 DSP cycles (17.1 μs) can be executed for 128 data words (25.6 μs) to identify the fluorescence signal.

An example of signal finding algorithm at DSP is illustrated in Fig. 18. The program looks for a set of signal edges T1 and T2 which maximize the S/N or $Q/\sqrt{BG}$. According to a Monte Carlo study, the charge resolution by this algorithm is 50 % for 10 photoelectrons (Q=10) and 20 % for 50 photoelectrons.

2.6.3 Signal Finder Module

A Signal Finder Module, which contains the front-end CSI, ADC and DSP, has been prototyped as the 3rd version (Proto-3) (see Fig.19).

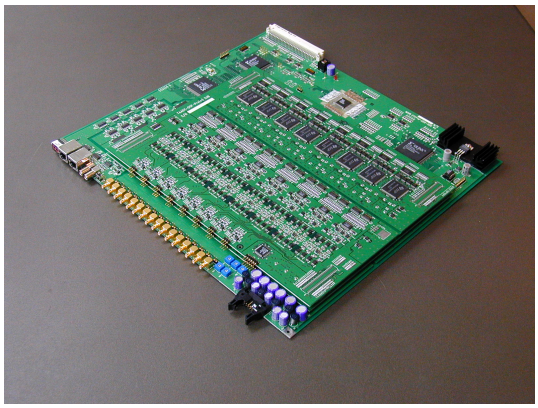

Fig. 19. Proto-3 module of signal finder. The height of the module is 9U but the depth of the module is extended to 50 cm.

The schematics of the module is shown in Fig.20. The module is implemented in a 9U VME board and contains 16 channels. The gain and offset of each channel can be corrected before the CSI with 16-bit DAC. The single range hybrid version of CSI is used for the present prototype (3rd version) with the 2-range scheme implemented.

Data transfer between the ADC and the DSP internal memory will be done through an 8-bit host port interface (HPI) of the DSP with a maximum speed of 20 MB/s and a buffer memory of 2 kB. ADC data tentatively buffered on the HPI memory without the DSP invention are transferred to internal circular data memory by the DSP program. The size of the circular memory is 32 k words, thus the data can be stored in the memory up to 6 ms (200 ns ×32 kW). Even for the inter site trigger which requires a long latency, a data copy operation is not required to the external memory because of such a enough

data memory on each DSP.

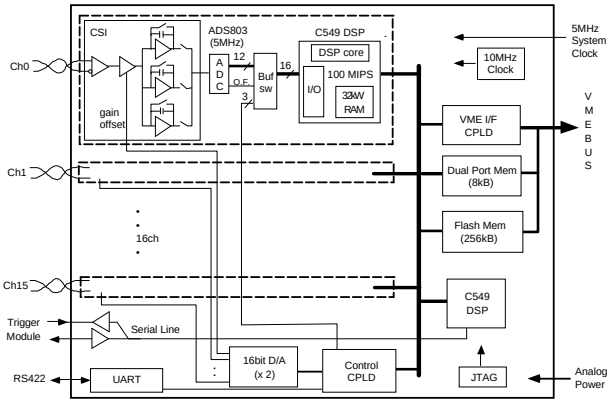

Fig. 20. Block diagram of the 16-ch prototype Signal Finder module. The module is implemented in a 9U VME board.

Between the ADC and the host port, 12-bit data and an overflow bit are transferred. In addition, 2 bits are transferred to a 2-bit counter, which is used to check the data sequence. Last one bit is reserved for H/L range control which is recognized in CSI. This is realized by comparison of the integrated charge on the CSI capacitance with the maximum charge of the high-gain range.

All the individual DSPs are controlled by another DSP, which collects the processed information (T1, T2, Q and S/N, etc.)(Fig. 18), and send them to the Track Finder trigger module through its serial lines at 50 Mbps. An easy-to-use commercial PC tool can be connected to the module via JTAG boundary scan port for debugging and monitoring of the DSPs. A dual port memory of 8 kB is used to exchange the data between the module and a VME master module. A Flash memory of 256 kB is included to store program and parameters. The whole system can be synchronized by using an external system clock of 5 MHz.

Sixteen modules of Proto-3, which corresponds to 256 input-channels, have been made and tested. The output noise fluctuation of CSI followed by the pipelined ADC is less than 2 photoelectrons, which is less than half of intrinsic night sky background fluctuation of $\sqrt{30} = 5.5$ photoelectrons in a PMT every integration time of 200ns. The ch-by-ch variation of the noise fluctuation is examined to be small. The noise originated from the Proto-3 circuit can be neglected. Also the signal finding algorithm and control among 16 DSPs on a module has been developed using assembler language dedicated to C549 DSP. We confirmed that the signal finding and data flow control can successfully work without any dead time on the way of the online data acquisition. Detailed results on trigger efficiency using the developed signal finding algorithm are shown later.[29)]

2.7 Trigger

2.7.1 Scheme

The overall signal to noise ratio (S/N) in view of a PMT is approximately given by:

$$\frac{S}{N} = N_e N_\gamma c \frac{1+\cos\theta}{4\pi R_P^2} e^{-r/\lambda_R} \left(\frac{\epsilon A}{4B\Delta\Omega}\right)^{1/2} \left(\frac{\Delta t_s}{\Delta t_I^{1/2}}\right)$$

$$\propto E\left(\frac{D^3}{d}\right)^{1/2} ,$$

explicitly showing the mismatch between the integration time Δt_I and the signal duration time Δt_S where A is the optical gathering area and λ_R is the Rayleigh scattering length, N_e is the number of electrons in the air-shower, and N_γ is the fluorescent yield. The measured S/N also

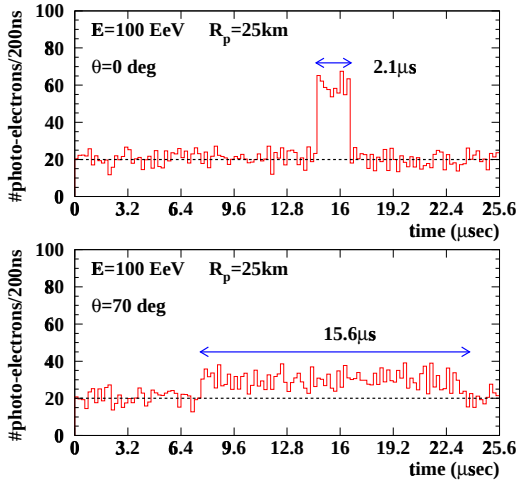

Fig. 21. Typical simulated PMT signals digitized by 5MHz-ADC for different event geometry of 10^{20}eV proton induced air-showers. Vertical (top) and deeply-inclined (70 degree; bottom) cases are shown. Impact parameter and night sky background are commonly assumed to be 25 km and 20 photoelectrons/200ns/PMT respectively.

depends on the primary energy of the air-shower and the optical factor where d and D are the diameters of the PMT and mirror aperture respectively.

For further optimization of S/N can be done by maximizing the factor of $(\Delta t_s/\Delta t_I^{1/2})$. A priori one does not know this Δt_s since it is event dependent. Events detected by the TA detector can generate pulses whose widths range from several tens ns to several tens μ s. Hence, to take full advantage of time integration in minimizing noise, we have employed an on-flight signal recognition with optimizing variable time filter by ch-by-ch parallel DSPs in order to trigger on nearby as well as distant events with optimum efficiency without strong bias for or against specific time duration of signal wave form. Assuming the optimized efficiency for triggering, we convert electron size N_e to energy in order to obtain an estimate for energy trigger thresholds. We take:[62)]

$E = 1.6 \times 10^{-9} N_e$, where E is the primary energy in EeV. Also assuming $r = R_P$ and the TA optical design, a crude estimate of the energy threshold is given by:

$$E_{th}[\mathrm{EeV}] = 10^{-4} \left(\frac{S}{N}\right) R_P^{3/2} e^{R_P/\lambda_R} \quad ,$$

where R_P is in km. This simple estimate suggests that the sensitive TA detector optics and readout devices should allow us significantly lower energy threshold of 10^{16}eV and larger detection aperture.

The rate of air-shower events with the energy of 10^{16} eV in the condition that the signal to noise ratio at least in one PMT should be more than one is estimated to be 0.2 Hz per camera with 256 PMTs equipped from Monte Carlo study. We can safely assume that the trigger rate from a detector station should be less than 10 Hz even taking into account faked triggers due to background pick-ups.

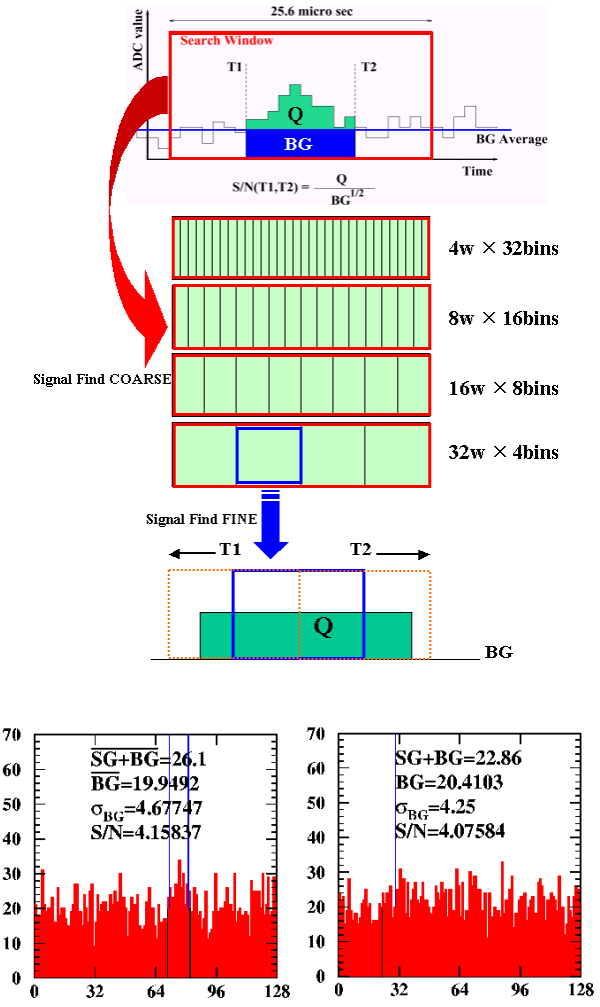

Fig. 22. Signal finding algorithm with coarse and fine search processes (top), demonstration of signal finding tests for short wave form (bottom left) and long one (bottom right). The two upper lines show true starting and ending times of input signal. The two lower lines show found ones.

2.7.2 Signal Finding

Even if using a series of high-performance DSPs, a sophisticated signal finding algorithm is indispensable. The DSP runs a signal finding algorithm (Fig.23 and 22) as follows:

1. Each SF-DSP defines the address region to search with the length of 25.6 μs corresponding to 128 words of ADC-data.
2. Maximize S/N(T1,T2)=Q/$\sqrt{B}$ changing T1 and T2 independently where Q is a charge sum between T1 and T2 and B is background averaged from average of past data not triggered.
3. In order to search the optimum S/N efficiently, each SF DSP performs two stages of search process, coarse search and fine one.
4. In the coarse search, the search window of 25.6 μs corresponding to 128 ADC-data is subdivided into four combinations of bins like 4 words×32 bins, 8 words×16 bins, 16 words× 8 bins, and 32 words× 4 bins. The DSP program finds a certain bin of which estimated S/N is larger than any others.
5. After the coarse search, the program starts a finer adjusting algorithm. It finds further increase of S/N as changing the starting and ending edges, T1 and T2, bin by bin around these found by the coarse search. And finally DSP program finds out the maximum S/N in the search window of 128 words.
6. Signal finding DSP send the determined T1,T2 , and Q to the dual port memory (DPM) to communicate with the module DSP.
7. The module DSP gathers the signal finding results from DPM and packs them into one serial packet.
8. The module DSP sends the serial packet of determined signal finding results to the event trigger track finding module via fast serial connection with a buffered serial port on the RxDSP of the TF module. The serial connection has a transfer rate is 50 Mbps.
9. The wave form data of 128 words are kept on the internal buffer memory of individual DSP. The buffer depth corresponds to 3 ms so that it can wait for the TF result as DAQ request in 3 ms. If there is no DAQ request from TF within 3ms after the search, the memory area is overwritten by new ADC data.

2.7.3 Track Finding

The TF module for event triggering essentially investigates the 3D-pattern in the (X, Y, T) space where X, Y stands for the PMT center position on the optical focal plane of the detector station and T for the T1 or T2. A prototype of TF has been developed (Fig. 23) and now it is under test. The data flow on the module is described as follows:

1. One TF module has 8 RxDSPs which have two buffered serial ports responsible for inputs from two SF modules respectively. Each buffered serial port on RxDSP receives each set of T1, T2, and Q synchronously every 25.6 μs.
2. The RxDSP quickly recognizes mutually connected in (X,Y,T) 3D-coordinates out of SF results in a

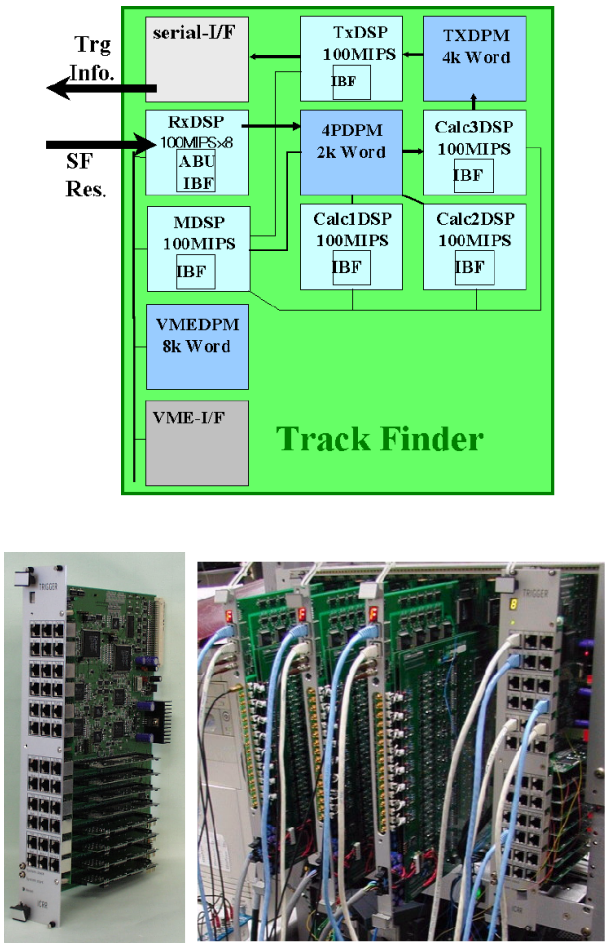

Fig. 23. Block diagram of Track Finder (top) and photograph of a prototype module of Track Finder and bench test connecting between the Signal Finders and the Track Finder (bottom).

pretrigger PMT cluster. And it calculates the total S/N for the cluster (cluster-S/N) from chosen sets of T1, T2, and Q.

3. The RxDSP sends out the data of the resultant cluster-S/N and all 16 sets of signal finding results to 4-port memory (CALCDPM) via the module bus. The transfer timing is well scheduled not to collide with each other on the module bus. Just after all RxDSPs finish transferring the cluster results, interrupt signals are sent to three DSPs (Calc1DSP, Calc2DSP, and Calc3DSP) for track finding calculation in order to inform them data-ready.
4. The Calc1DSP judges pretrigger with all 16 cluster-S/Ns. The total S/N with only signals in clusters mutually connected out of 16 clusters on one camera in the 3D-coordinates is calculated similarly to the previous S/N extracted from a pretrigger cluster. The total S/N in one camera is used to finally determine the pretrigger. The pretrigger threshold must be decided from detailed Monte Carlo studies or real pilot observations.
5. Calc1DSP also determines the center of gravity (c.o.g.) of the 3D-pattern for pretriggered events.
6. Calc2DSP searches track of 3D-pattern of (X,Y,T) again (Fig. 24) from the c.o.g. using all signal finding informations including wider time region.
7. Calc3DSP calculates the total S/Ns from the selected patterns by Calc2DSP. After that, it finds the largest S/N from signal informations close to the optimum track (track-S/N) and judge the final trigger decision. The result of the trigger judgment is sent to a dual port memory (TXDPM) followed by TxDSP.
8. TxDSP always watches the trigger judgment stored on TXDPM. Once it obtains the trigger judgment, the TxDSP makes a serial packet to inform the result to the corresponding SF modules. The serial packed has a header information including the identification of the SF module and window, which indicate the addresses of memories of data contributed to the triggered event. The TxDSP send the packet data onto serial interface port. Finally SF module receives the distributed SF module and window identifications with a DAQ request.

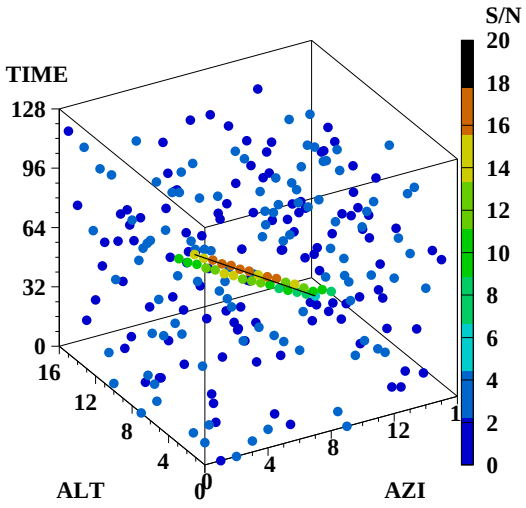

Fig. 24. Simulated results of signal finding for 10^{18}eV air-shower and night sky background.

We have confirmed the data flow in the connection between the SF and TF prototypes are well controlled synchronously (Fig. 23). From the detailed Monte Carlo studies, we have investigated the efficient trigger condition (Table VI). The track-S/N is totally biased by approximately 4 due to maximizing S/N in the series of Signal Finding, cluster-S/N, and track-S/N algorithms. For instance, calculated track-S/N only from simulated night sky background has a distribution of which mean value is about 5. If we adopt $S/N > 7$ as the trigger threshold cut, the background contamination can be reduced by factor of 4000, In the same condition, the trigger aperture for air-shower events with the primary energy of 10^{20} eV using only one detector station is estimated to be 6.6×10^4 km^2 sr, which corresponds to the

Table VI. BG rate and trigger aperture vs trigger condition

S/N cut	BG (Hz) in Camera	Trigger Aperture ($km^2 \cdot sr$) for Proton with One Station			
		10^{17} eV	10^{18} eV	10^{19} eV	10^{20} eV
7	10	5.6×10^2	6.5×10^3	2.6×10^4	6.6×10^4
8	2	4.8×10^2	6.0×10^3	2.5×10^4	6.1×10^4
9	0	4.0×10^2	5.6×10^3	2.4×10^4	5.9×10^4

detection area of 60 km radius around one station. The sophisticated 3D-pattern track finding algorithm and the DSP assembler program are now under developing.

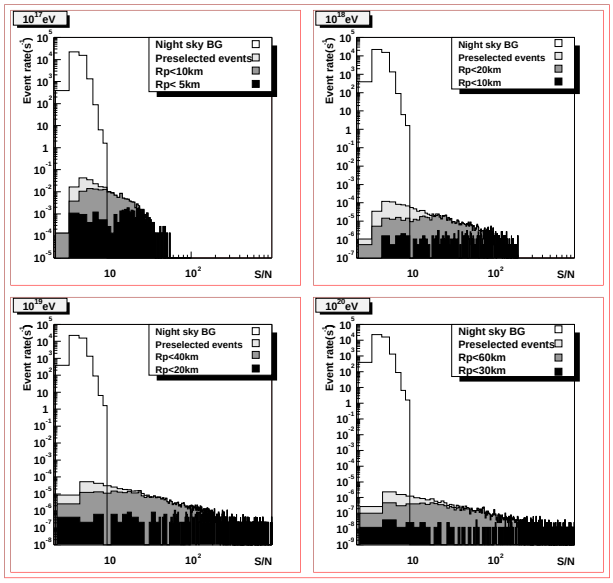

Fig. 25. BG and cosmic proton event rate as a function of total S/N in connected PMTs

2.8 *Data Acquisition*

An event size distribution of one TA station for the air shower events with energies above 10^{19}eV is shown in Fig. 27. The size is less than 1.5 kBytes for 90 % of the event. The event rate of air shower with energy more than 10^{16}eV is less than 0.3 Hz per station. Even we assume a maximum trigger rate of 10 Hz caused by the Cerenkov light of low energy showers and muons, the maximum data transfer rate is 15 kBytes/s. This rate of event building can be comfortably achieved by the Ethernet technology.[30] An overall scheme of TA event building is shown in Fig. 26. Once the signal finder module receives a DAQ request from the trigger, the stored data in the internal memory of DSP are sent to the event builder computer through a VME bus and VME/PCI adapter. Data from 512 channels (two telescopes) are gathered into one VME crate consisting of 8 units of 64ch signal finder modules and 1 VME/PCI adapter card. The adapter will send the combined data into 1 front-end network PC. The switching HUB is to merge the fast-ethernet data packets from 20 network PCs into the

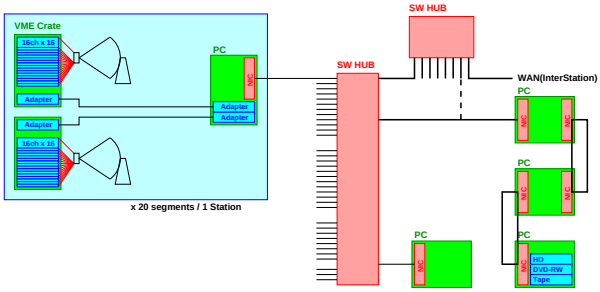

Fig. 26. TA data acquisition system.

event builder PC by Giga-bit ethernet technique. An additional 2 PCs connected by the Giga-bit ethernet LAN will form a DAQ computing farm. The DAQ farm is responsible for the event building, filtering, quick online analysis and monitoring, and the maintenance of online calibration database.

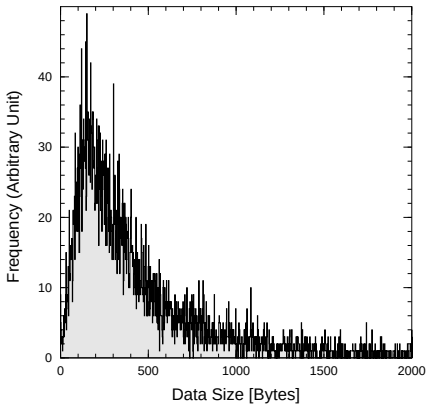

Fig. 27. Data size for air shower event.

§3. Event Reconstruction

3.1 *Geometrical Reconstruction*

The air shower reconstruction is divided into a series of steps which fall into two major divisions: geometric reconstruction and shower profile reconstruction. Briefly, the geometric reconstruction begins with determining the shower-detector plane from the PMT hit pattern. Once this plane is determined, the remaining parameters for an air shower trajectory are the impact parameter R_p and incident angle Ψ in the plane. The relationship between these parameters and the PMT hit times can be expressed as:[27]

$$t_i = t_0 + \frac{R_p}{c}\tan\theta/2$$

where, c is the speed of light, t_i is the i-th PMT hit time, θ_i is the emission angle from the track to the i-th PMT;

θ_i is related to Ψ by:

$$\theta_i = \pi - \Psi - \chi_i$$

where χ_i is the PMT elevation angle in the plane. t_0 stands for the time the shower front plane pases through the detector. For short tracks, the above function $t_i(\theta_i)$ is difficult to distinguish from a straight line. In that case, R_p and Ψ are not independently identified. In order to decouple these two parameters, a long track length in angular space is necessary. The resolution of both R_p and Ψ depends strongly on the track length.

If a shower is seen simultaneously by two detector stations, a shower-detector plane for each detector station can be determined and the intersection of those planes defines the shower trajectory. With this stereo reconstruction, no timing information is needed except to distinguish between upward and downward tracks. However, stereo reconstruction becomes difficult when the opening angle between the planes is too small. This happens when a shower falls in a narrow region along the line between the two detector stations or is very distant from two detector stations. Except for those small opening angle events, the stereo reconstruction usually yields smaller errors and less pronounced tails in error distribution than the monocular reconstruction.

3.2 Atmospheric Calorimetry

The photo-electron number N^i_{pe} counted in the i-th PMT is related to the energy loss E^i_{loss} of the air shower during its passing through the atmosphere within the i-th PMT's FOV by:

$$N^i_{pe} = E^i_{loss} \cdot \eta(\rho, T) \cdot \frac{A_i}{4\pi R_i^2} \cdot C^i_{Air} \cdot \epsilon^i_{Opt} \qquad (3.1)$$

where η is the yielding efficiency of the atmospheric scintillation as a function of the atmospheric density ρ and the temperature T. A_i is the effective area of the light collector taking into account obscurities due to the structure supports of the telescope and the imaging device, which depend on the position of the PMT's view point. R_i is the distance between the i-th PMT and the air shower. C^i_{Air} stands for the air fluorescence extinction due to scattering with atmosphere. This is quite important and described in more detail later. ϵ^i_{Opt} is the efficiency of the optical system including the reflection of the mirror, the transmittance of the optical filter, the PMT quantum efficiency, the dead-space correction of the PMT array of the imaging device, and so on.

The observed number of photo-electrons in each PMT is given by Eq. 3.1. The total observed energy deposit E from the air shower is obtained by summing all E^i only from real measurements and simple geometrical calculations, in principle, but not from any *ad hoc* correction by Monte Carlo detector simulation. This is one of beauties of cosmic air shower observation with air fluorescence technique.

Finally the primary cosmic ray energy E_0 can be determined after totally correcting E by a factor of C_{tot}:

$$E_0 = C_{tot} \cdot E\,,\ E = \sum_i^{all} E^i\,. \qquad (3.2)$$

The total correction C_{tot} depends on the following facts:

- Energy deposit of air shower without the detector FOV, which is partially carried by muons, hadron, neutrino, and so on.
- Energy loss through interaction channels which do not contribute to the scintillation light like nuclear scattering.
- Detector gap and doubly counting photons.
- Contamination from Cerenkov lights.
- Detector status, trigger, and selection efficiencies.
- etc.

In order to determine the corrections due to physics process and Cerenkov light, realistically, comparison of useful control data with Monte Carlo simulation extrapolated from accelerator data can be used. Using the reconstruction method as above described, we can obtain longitudinal air shower development, which is the direct information to determine the first interaction point of the primary cosmic ray particle in the slant depth. Experimentally, the parameter of the slant depth at the maximum shower development X_{max} is often used where the statistical power is good.

3.3 Atmospheric Monitor

3.3.1 Traditional Lidar Method

In order to investigate the atmospheric extinction of lights, the Lidar technique is often used in the fields such as environmental science or air polution studies. Lidar states the abriviation of Light Detection and Ranging. Lidar systems widely used for remote sensing of the atmosphere consist of a pulsed laser source and a light receiver to measure a time-profile of the return signal.

For a monostatic single-wavelength pulsed lidar, the assumed basic govering form is the single-scattering lidar equation:

$$P(r) = P_0 \frac{c\tau}{2} A \frac{\beta(r)}{r^2} \exp\left(-2\int_0^r \alpha(r')dr'\right) \qquad (3.3)$$

where $P(r)$ is the instantaneous received power at the t, P_0 the transmitted power at time t_0, c the velocity of light, τ the pulse duration, A the effective system receiver area, $r = c(t - t_0)/2$ is the range, and $\beta(r)$ and $\alpha(r)$ are, respectively, the volume backscatter and attenuation coefficients of the atmosphere. A more convenient signal variable is the logarithmic range adjusted power, defined as:

$$R(r) \equiv \ln(r^2 P(r)) \qquad (3.4)$$

Eq.1 may be expressed in a system-independent form:

$$R(r) - R(r_0) = \ln\frac{\beta(r)}{\beta(r_0)} - 2\int_{r0}^r \alpha(r')dr' \qquad (3.5)$$

where r_0 is a given constant reference range.

The differential equation corresponding to Eq.3 is:

$$\frac{dR}{dr} = \frac{1}{\beta}\frac{d\beta}{dr} - 2\alpha \tag{3.6}$$

a solution to which evidently requires knowing or assuming a relationship between β and α whenever $d\beta/dr \neq 0$. On the other hand, if the atmosphere is homogeneous so that $d\beta/dr = 0$, the attenuation coefficient can be expressed directly in terms of the signal slope:

$$\alpha_{hom} = -\frac{1}{2}\frac{dR}{dr} \tag{3.7}$$

This is the basis of the slope method of inversion,[31)32)] in which typically the slope of the least squares straight line fit to the curve $R = R(r)$ is used as the best estimate of dR/dr over any interval where R itself appears to be nearly a straight line. Unfortunately, assumptions like this appear not to be well justified for many situation of interest, e.g., under conditions of dense cloud, fog, smoke, and dust. Even under the relatively stable conditions prevailing in fogs, significant local heterogeneities occur. For example, the spatial variation of fog drop concentrations is often quite large, ranging up to 2 orders of magnitude for certain size categories [34)].[35)] Such microstructure variation along the lidar beam path could easily lead to relatively large fluctuations in $d\beta/dr$, hence invalidating local application of the slope method. The same criticism applies to the so-called ratio or slice method of inversion [36)],[37)] which is merely an extremely close variant of the slope method as applied to successive range intervals [38)].[39)]

From several observational and theoretical studies that show that under a wide range of circumstances for which particulate backscattering dominates that due to atmospheric gases, i.e., roughly for hazy, cloudy, or foggy conditions, β and α can in fact be related approximately according to a power low of the form:

$$\beta = const\ \alpha^k \tag{3.8}$$

where k depends on the lidar wavelength and various properties of the obscuring aerosol. Reported values of the exponent are generally on the interval $0.67 \leq k \leq 1.0$. [39)40)41)42)] If Eq.6 is assumed, Eq.4 becomes an elementary structure of the Bernoulli equation:

$$\frac{dR}{dr} = \frac{k}{\alpha}\frac{d\alpha}{dr} - 2\alpha \tag{3.9}$$

and a well-known form of the solution may be obtained:

$$\alpha = \frac{\exp((R(r) - R(r_0))/k)}{\alpha^{-1}(r_0) - \frac{2}{k}\int_{r0}^{r}\exp((R(r') - R(r_0))/k)dr'} \tag{3.10}$$

This solution has serious divergent problem due to the small differences in the choice of boundary value $\alpha(r_0)$ which may make the denominator of the righthand side of Eq.9 zero.

One can select a different and more appropriate solution form than Eq.9 using a different boundary condition .[43)] In terms of a reference range r_m, the solution is generated for $r \leq r_m$ rather than for $r \geq r_0$ as before.

$$\alpha = \frac{\exp((R(r) - R(r_m))/k)}{\alpha^{-1}(r_m) + \frac{2}{k}\int_{r}^{r_m}\exp((R(r') - R(r_m))/k)dr'} \tag{3.11}$$

As r decreases from r_m, α is now determined as the ratio of two numbers that each become progressively larger, so that stability and accuracy are easy to maintain. The form of the denominator also indicates that the dependence of the solution on $\alpha(r_m)$ decreases with decreasing r.

This solution is turned out to be applicable for the analysis of lidar observations collected only in very turbid atmospheres. There is the more general solution ,[44)] which is also applicable to mildly turbid atmospheres where both aerosol (Mie) and molecular (Reyleigh) scatteres must be considered in the analysis. This has led to a simple numerical scheme for the computer analysis of lidar measurements. The method uses one further simplifying assumption that the extinction-to-backscattering ratio for aerosols, $C_{as} = \alpha_{as}(r)/\beta_{as}(r)$, remains constant with range. It essentially states that the size distribution and composition of the aerosol (Mie) scatteres are not changing with range from the lidar, and that variations in backscattering from aerosols are due to changes in their number density.

In relatively clean atmospheres, the basic result of the analysis is the aerosol (Mie) backscattering cross section, and the aerosol extinction now becomes dependent on an accurate knowledge of the extinction-to-backscattering ratio .[45)] Also, even for moderately turbid atmospheres, the analyses will be sensitive to both the extinction and back-scattering properties of the aerosols so that the lidar system must be accurately calibrated and the extinction-to-backscattering ratio must be reasonably well established. However, it is reported that the cirrus extinction-to-backscattering ratio depends on crystal shape, size, and orientation, and it can vary by a factor of 2 or more as a function of range .[46)]

We have already taken data for the back-scatter lights observation using the traditional lidar method proposed by Klett.[43)] An example for one night observation is shown in Fig. 3.3.1.

3.3.2 New Simultaneous Method[47)]

As described above, we would better to take another approach for the purpose of the air-shower energy correction in stead of lidar systems which are widely used for remote sensing of oceans and the atmosphere, although we can think it as hints for the develoment of our system. It is preferable to determine the attenuation coefficient only from the measurements without assuming strong *a priori* inputs which may limit the condition of target objectives. A new simultaneous method using multiple detector stations as scattered laser light receivers has been proposed.[47)]

First of all, we reconstruct the arival direction and the impact point of the air-shower axis for each triggered air-shower event in the online data acquisition system for the air-fluorescence detection. In the process, we have to filter triggered events to quickly avoid apparent con-

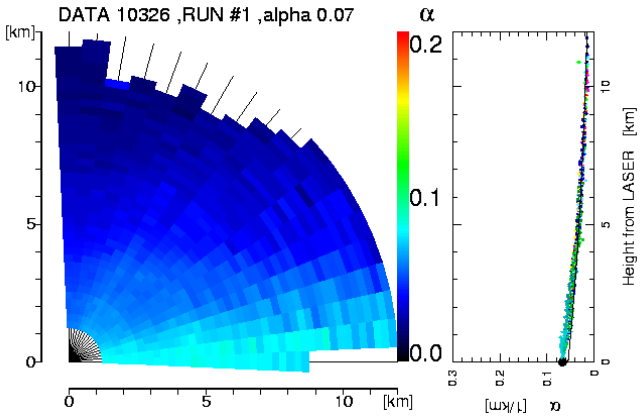

Fig. 28. Lidar result using the traditional Klett's method.

taminations from night sky backgrounds and Cerenkov lights from lower energy air showers.

Now we consider a laser monitoring system which consists of mutiple sets of laser sources and light receivers to reconstruct the profiles of the signals scattered at a local area on the reconstructed air-shower axis in the atmosphere. The layout assumed here is the T.A. with enhancement of air-fluorescence detection as shown in Appendix A. Each of seven eyes has each laser set which shoot pulses in any direction over the solid angle of 2πsr. We start with a generalized lidar equation modifing Eq.1. In the case that a light pulse is emitted by a laser source of the i-th eye, scattered by an atmospheric area at the position of a given slant depth X along the reconstructed air-shower axis, and detected by telescopes in the j-th eye, the received power from a laser light pulse scattered at a given X is expressed by:

$$P_{ij}(X) = P_{i0}\frac{c\tau_i}{2}\frac{A_j(X)}{r_j^2}S_{ij}(X)T_i(X)T_j(X) \qquad (3.12)$$

where $P_{ij}(X)$ is the instantaneous received power at the t for the light from a laser in the i-th eye and with telescopes in the j-th eye, P_{i0} the transmitted power of the laser in the i-th eye at time t_0, τ_i the pulse duration of the light from the laser i, $A_j(X)$ the effective system area of the telescope in the eye j, r_i and r_j are the ranges from the laser i and the eye j to the position of X respectively, $S_{ij}(X)$ is the volume scattering coefficient with the scattering angle between the laser i and the eye j, and T_i is the transmittance of the atmosphere in the range between the scatterer volume at X and the eye i. In a real procedure, the direction of laser light is changed as changing X on the air-shower axis and data sets of the received power profiles with different values of X are stored as computer files associated with the fluorescence data taken for the air-shower event.

Once we determine the geometry of the shower axis and fix the position of the scatterer volume on the measured shower axis, we can obtain m^2 measurements of P_{ij} if we have m available eyes with the laser units. In order to algebraically solve the equations, it is more convenient to define the logarithmic range-adjusted powers for the m^2 measurements similarly with Eq.2:

$$R_{ij} \equiv \ln\left(\frac{P_{ij}}{P_{i0}\frac{c\tau_i}{2}\frac{A_j}{r_j^2}}\right) \qquad (3.13)$$

so that the unknown coefficients can be related with the measurements, given by:

$$R_{ij} = \Sigma_{ij} + \Gamma_i + \Gamma_j \qquad (3.14)$$

where $\Sigma_{ij} \equiv \ln S_{ij}$ and $\Gamma_i \equiv \ln T_i$, $(1 \le i, j \le m)$. The spot size of the laser light pulse is expected to be several meters at 10 km distance if it has the beam spread of approximately 0.5 mrad. Also the time duration of the pulse is about 5 ns, which is equivalent to the path of 1.5 m. Once we can reasonably neglect the spatial structure within 10 meters and the time variation within 5 ns for a given scatterer volume at a distance, the scattering coefficient depends only on the scattering angle. As a result, we can use the following constraints:

$$\Sigma_{11} = \Sigma_{22} = \cdots = \Sigma_{mm} \quad \text{and} \quad \Sigma_{ij} = \Sigma_{ji}\ (i \neq j) \qquad (3.15)$$

Using the above constraints, R_{ij} is turned out to be symmetric in terms of the i and j subscripts so that the number of independent equations out of the simultaneous system 12 is derived to be $m(m+1)/2$. On the other hand, the number of unknown variables in Eqs.12 can be calculated to be $m(m+1)/2+1$, which is just one more than the rank of the simultaneous equation system 12. Figure 3.3.2 shows the schematic layout of this examples,

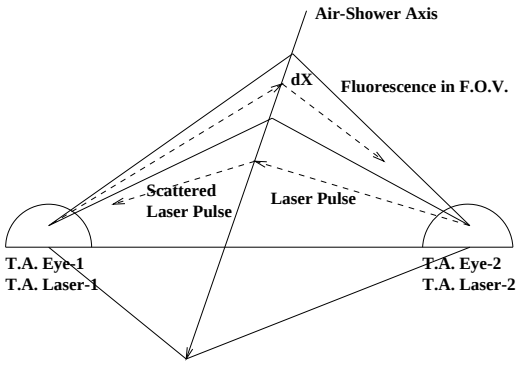

Fig. 29. Reconstruction geometry for an air-shower in stereo with the T.A. eye-1 and eye-2.

where three lidar units are set at the center of two adjacent telescope-eyes located at the distance of 30-40 km.

We need to introduce an input from outside of the our measurement and atmospheric laser monitoring systems. Since the intensity of the laser light pulse is rather controlable, it may not be difficult to detect laser light pulses with telescopes in three or more eyes even if air-fluorescence lights from the real air-shower event can be detected only by one eye. The scattering factor S_{ij} consists of two contributions by atmospheric molecules (Rayleigh scattering) and by natural and man-made aerosol particles (Mie scattering) which can be ex-

pressed by:

$$S_{ij} = S_{ij}^R + S_{ij}^M \tag{3.16}$$

where the Rayleigh scattering term is exactly calculatable and only the Mie scattering term is unknown, although the Mie contribution is reported to be rather small (<20%). From the atomospheric monitoring with three or more eyes, we can eliminate one unknown variable $S_{\alpha\beta}^M$ for a certain set of α and β ($\alpha \neq \beta$) in Eqs.22 or 10 using a fit of a theoretical expectation curve to other S_{ij}^M ($i \neq \alpha, j \neq \beta, i \neq j$). Fig. 3.3.2 shows the expectation curve of the Mie scattering factor as a function of the scattering angle from the MODTRAN atmospheric simulation assuming the standard desert model [22]. As we see, in the forward ($\theta < 30°$) and backward regions ($\theta > 150°$) the scattering factor rapidly changes and has a strong dependence of the wind speed due to the change of the size parameter of the aerosol as a function of the scale height. However, in the region between $30° < \theta < 150°$ the shape of the function does not change rapidly as θ changes and is not influenced so much by the wind speed. Fortunately, the scattering angle between two of all triggered eyes falls in that region for many air-shower events. Once we succeed in the elimination of one unknown variable, we can resolve the longitudinal shower profile using the same procedure as that in the stereoscopic case. We should note that we have to carefully evaluate the systematics introduced by the variable elimination using the fit to the scattering factor as a function of scattering angle using the Monte Carlo simulation and crosschecks with data.

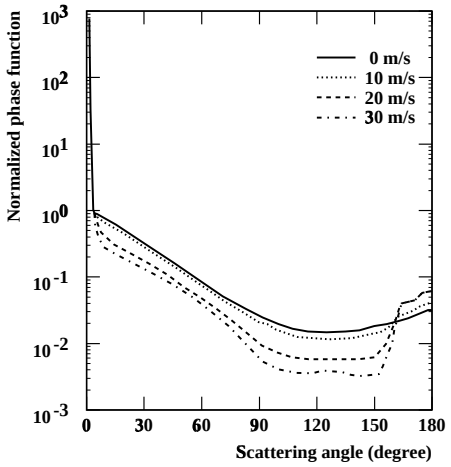

Fig. 30. MODTRAN output for the Mie scattering cross section as a function of scattering angle varying the wind speed.

Table VII. The Cosmic ray hadron annual event rate detected and reconstructed by the TA detector. The cosmic ray flux measured by AGASA is assumed.

Energy			Event rate [yr^{-1}]
3×10^{18}eV	$\leq$ E $\leq$	10^{19}eV	11150
10^{19}eV	$\leq$ E $\leq$	3×10^{19}eV	1973
3×10^{19}eV	$\leq$ E $\leq$	10^{20}eV	354
10^{20}eV	$\leq$ E		70

§4. Monte Carlo Performance

The Event Generator calculates signal strength produced by atmospheric fluorescence light emission from an Extensive Air Shower (EAS) with a given geometry, and builds simulation events by calculation of number of photoelectrons in every channels of a PMT camera in each mirror. It involves the longitudinal profile of an EAS, the models of the atmosphere, the air fluorescence yield, and the detector optics. Simulation of actual pulses with superposing the night sky background is performed in the second subset, the Signal and Background Pulse Generator. The shower development is basically calculated by the modified Gaisser-Hillas function.[62] The Generator also has another option to use numerical functions fitted by the shower profile simulated by the Corsika and/or AIRES[56] Monte Carlo package instead of using the Gaisser-Hillas formula.[62] In this option X_1 and X_{max} are given directly from the external Monte Carlo shower simulation package.

4.1 Stereo Aperture

The air shower events are reconstructed when at least 6 PMTs of one or two neighboring telescopes are fired 4 σ above the night sky background. The total number of detected photoelectrons and the length of the reconstructed track are investigated with Monte Carlo simulation for protons with various energies, which have at least one reconstructed track.

In order to define the stereo aperture of TA, we required that at least two stations have a well reconstructed track, both of which extend more than 5° in the FOV. The aperture obtained with this condition is plotted in Fig. 31 for 10^{18} – 10^{21}eV protons. It is $\sim$ 65,000 km^2 sr for 10^{20}eV protons, which indicates that the shower as far as $\sim$ 60 km away from the closest station can be detected and reconstructed for 10^{20}eV protons. The acceptance for the 10^{19}eV proton is not concentrated in the vicinity of each station but rather uniformly distributed near the center of the TA site. The expected event rates are listed in Table VII. The events with energies beyond 10^{20}eV are detected at 70 events/year assuming the flux of super GZK events measured by AGASA. Now the question is how well we will be able to distinguish the different models to resolve the long-standing mystery of their origin with the expected power of the detectors. Our observations consist mainly of the energy spectrum, the primary mass composition,

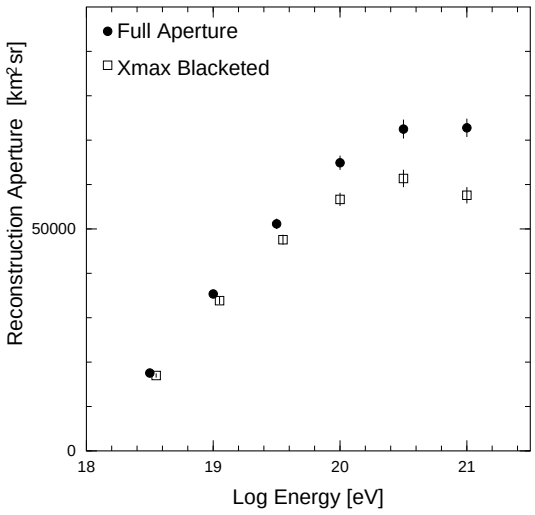

Fig. 31. The stereo aperture of TA.

and the arrival directions of the energetic particles. The proposed models have their own predictions that can be measurable by our detector. Fig. 32 illustrates our typical discrimination power by measurement of the energy spectrum. It is clearly seen that the spectrum is reconstructed well enough to show whether the GZK cutoff indeed exists or not.

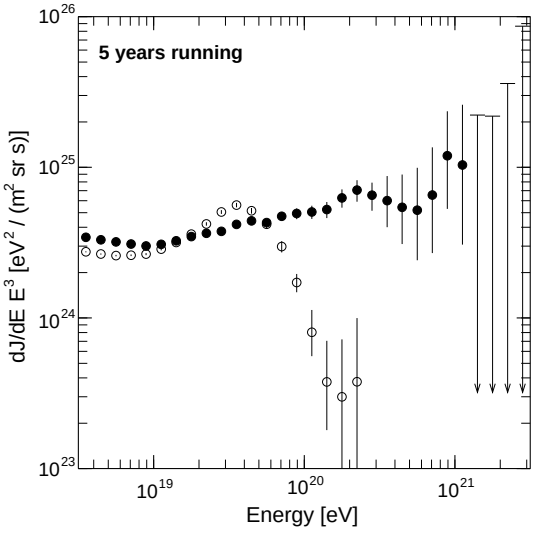

Fig. 32. 5 years observation of the energy spectrum by the Telescope Array. Closed circles show the case if the spectrum simply extends well beyond 10^{20}eV[1] while open circles represent the "standard model" with the GZK cutoff assuming the sources are distributed homogeneously in the Universe.[5]

The newly proposed scenarios such as the Top Down models and the neutrino Z-burst model have predicted the specific population of cosmic rays dominating above 10^{20}eV which would be created by decay of the supermassive particles[9] or cascading initiated by superhigh energy astrophysical neutrino beams.[10,11] In this case, the TA detector will see the new component extending well beyond 10^{20}eV. As illustrated in Fig. 33, the observation for 5 years would be enough to detect these superhigh energy particles that become predominant after the GZK cutoff. The dip structure appears at 10^{20}eV if the low energy component presumably radiated from the radio galaxies, the most favorite candidates of the high energy cosmic ray emitters, exhibits the GZK cutoff as expected from our standard GZK picture. This would be a strong signature to suggest the Top Down/Z-burst models that are necessarily associated with the hard energy spectrum ($\sim E^{-2}$) extending to 10^{21}eV or even higher.

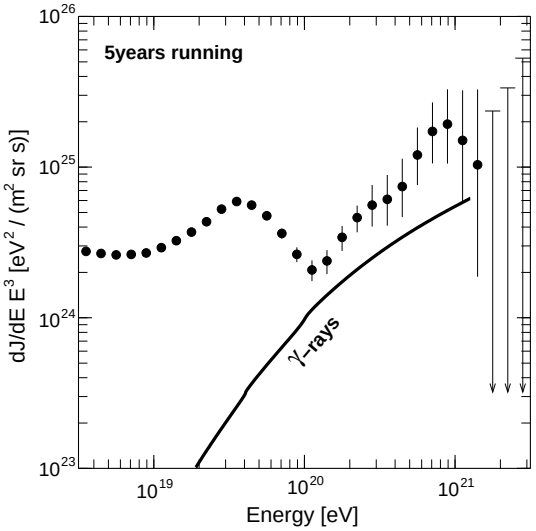

Fig. 33. 5 years observation of the energy spectrum by the Telescope Array if the highest energy cosmic ray has a new population dominating above 10^{20}eV as predicted by the Z-burst or Top Down models. The solid curve represents the primary γ-ray intensity predicted by the Z-burst model.[51]

It should be noted that these models lead to primary γ-ray flux that is comparable or higher than nucleon intensity with energies above 10^{20}eV. As described in §4.3, our capability to measure the longitudinal shower profile gives significant sensitivity to statistically identify primary γ-rays if they exist. As shown in Fig. 33, our sensitivity would be good enough to detect the predicted γ-rays component if these models are correct.

Because trajectories of γ-rays would not be bent by any magnetic field, the most energetic particles are able to be traced back exactly to their emission point where one can find counterparts of the astronomical objects like AGNs or GRBs. Five years observation by the TA detector is expected to detect $\sim$ 250 events with energies greater than 10^{20}eV, and at least 30 % of them is predicted to be γ-rays. This indicates that we will have a fairly good chance to see many triplets or more dense event clusters if the possible small-scale anisotropy AGASA has seen is real. Whether we find astronomical counterparts in their directions and whether the counterparts are within the GZK horizon or not would be

direct evidence to identify the highest energy cosmic ray sources.

4.2 Angular and Energy Resolutions

For the air fluorescence method, there are 3 major factors to influence the resolution of measurement.

- Event reconstruction
- Atmospheric correction
- Pixel calibration (optics and electronics)

The accuracy of event reconstruction is important for all the observables such as the energy, the arrival direction and the shower maximum X_{max}. The atmospheric correction and the pixel calibration are most relevant for the resolution of energy measurement. Besides the resolution, we need to estimate the accuracy of the measurement in absolute scale, which is particularly important for the energy measurement.

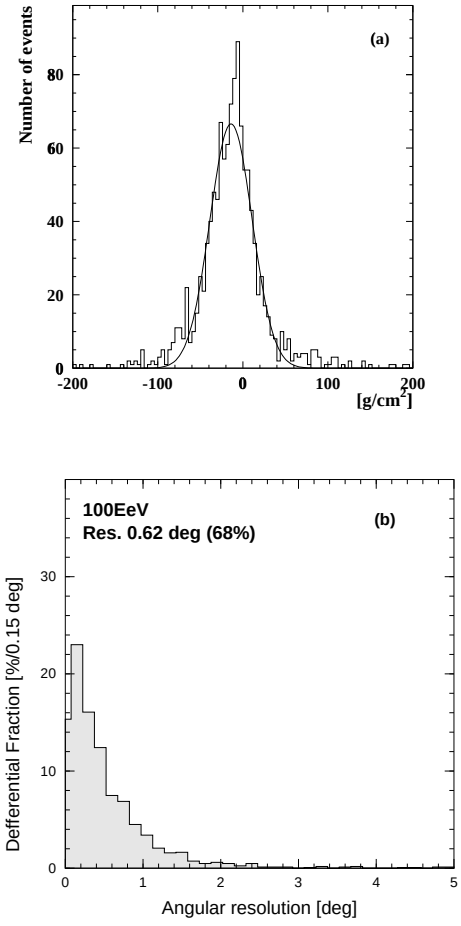

Fig. 34. (a) The X_{max} resolution; $X_{max}^{rec} - X_{max}^{gen}$, (b) The distribution of the opening angle between the generated and reconstructed vectors of the arrival direction, obtained for 10^{20}eV protons generated by CORSIKA.

The accuracy of event reconstruction is estimated by comparing the value obtained by the event reconstruction with the value used for the event generation. The original X_{max} used for the generation, X_{max}^{gen}, is determined by fitting the generated shower profile with Gaisser-Hillas function We use superscripts ^{gen} and ^{rec} for the value used for the generation and the value obtained by the reconstruction.. The reconstruction resolution of X_{max} and the arrival direction is plotted in Fig. 34 for 10^{20}eV protons generated by the CORSIKA simulation code. All the events satisfying the stereo condition are used except that a few events with large χ^2 in the fitting are excluded. The large χ^2 events mostly correspond to the sizable contributions from the Cherenkov emission. These events amount less than 3% of the total sample and they can be recovered by refining the event reconstruction algorithm in future. It is remarkable that the X_{max} and angular resolution distribution have a well controlled shape without a long tail.

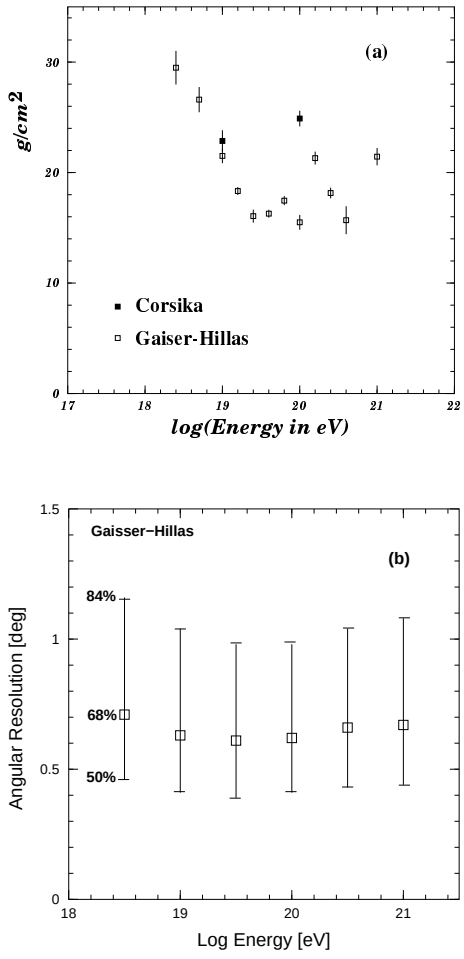

Fig. 35. The energy dependence of (a) X_{max} resolution and (b) angular resolution.

In order to determine the reconstruction resolution, we fitted the distribution of X_{max} by the Gaussian. The angular resolution is determined from the integral distribution (Fig. 34(c)) as the point below which 68% of the events are contained. The resolution obtained this way is plotted in Fig. 35. It includes the effect of shower fluctuation, the photoelectron statistics and the system-

atics originated from the fitting procedure. In tne same figure, the resolutions obtained for 10^{18}–10^{21}eV protons are plotted.

As described in § 3.2, the energy determination is based on the calorimetric energy integral, which leads to elimination of unknown systematic uncertainty concerning the hadron interactions at extremely high energies. Figure 36(a) shows the energy resolution distribution obtained for 10^{20}eV protons generated by the CORSIKA simulation code. As we expected, it is well represented by the Gaussian distribution, which is crucial for a reliable measurement because the cosmic ray energy spectrum is sharply falling with energy. The resolution is $\sim \pm 6$ % over the wide energy span from 3×10^{18} to 10^{21}eV as shown in Fig. 36(b).

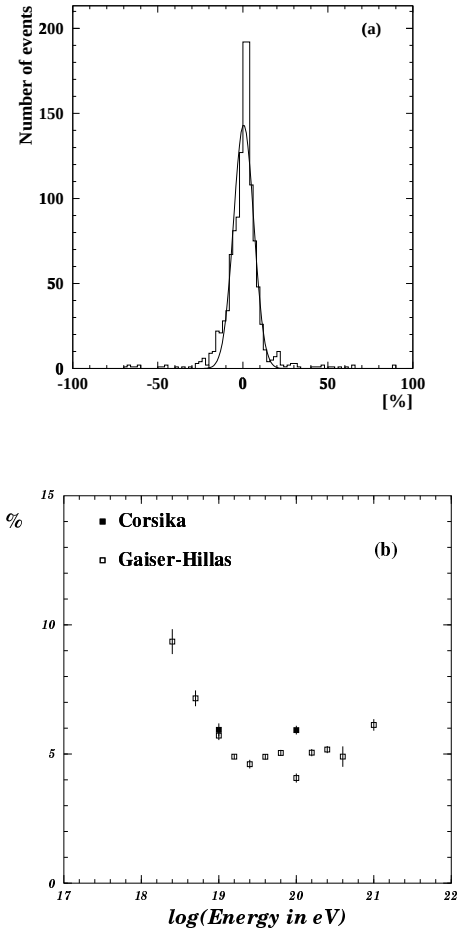

Fig. 36. The Energy Resolution distributions;$(E^{rec}-E^{gen})/E^{gen}$ (a) and the resultant energy resolution as a function of shower energy (b).

As one can see in Eq. (3.1), the systematic uncertainties on the energy estimation mainly arise from the following factors:

- The first term, the detector efficiencies are measurable/predictable by our detector calibration and the detector Monte Carlo simulation. The overall uncertainty is estimated to be 10 %.
- The second term, the fluorescence yield η has been well measured by a laboratory experiment.[75] The yield for low energy electrons below 1 MeV is not quite understood, however, and the uncertainty is given as $\sim$ 10 %.
- The energy loss per unit atmospheric length E_{loss} is based on our knowledges of the particle interactions. It is known to have slight dependences on the age of EAS cascade and the primary mass initiating an EAS. The canonical number for electromagnetic cascades is 2.0 MeV/(g/cm^2). The modified Gaisser Hillas function gives 2.31 MeV/(g/cm^2). The CORSIKA full Monte Carlo simulation gives 2.19 MeV/(g/cm^2) with some dependences on the primary particle mass. The uncertainty have been estimated to be $\sim$ 5 % mainly because of the dependences on the shower age and the threshold energy of secondary electrons and photons in the simulation.
- Energies carried by penetrating particles like neutrinos and muons must be taken into account to estimate primary energy E_0 of cosmic rays from the air shower energy E_{sh} determined by Eq. (3.2). The full Monte Carlo simulation can calculate the fraction of these missing energies. The CORSIKA simulation gives this fraction as

$$\frac{E_{sh}}{E_0} = 0.959 - 0.082 \left(\frac{E}{10^{18}\text{eV}}\right)^{-0.15} \quad . \quad (4.1)$$

  for average behavior of protons and irons. Uncertainty of 5 % has been estimated due to lack of knowledge of primary mass.
- The last term related on the atmospheric extinction is expected to make major contributions to the overall uncertainty on the energy estimation as discussed next.

The energy resolution may be significantly affected by the atmospheric correction. In Fig. 37, we show a scatter plot of the extinction caused by the Mie scattering vs the distance from the shower luminous center to the station for 10^{20}eV protons. As shown, the average extinction by the Mie scattering reaches 0.7 for showers more than 40 km away, but it saturates beyond this limit.

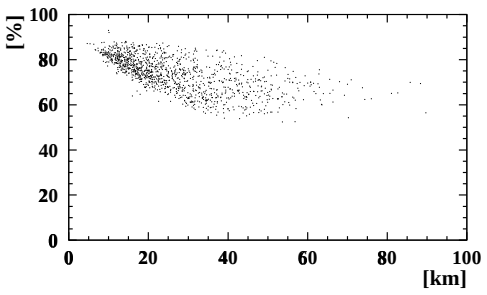

Fig. 37. Scatter plot of the distance from the shower luminous center to the station vs Mie extinction. It is plotted for the nearest station to the shower center.

Table VIII. Estimated systematic uncertainties of energy measurement

Item	Error	Comments
Number of photoelectrons	5%	
Fluorescence yield	10%	inc. pressure uncert.
Distance to shower	5%	error in R^2
Detection efficiency	10%	5% for mirror, 5% for filter, 8% for PMT, 3% for obscuration.
Energy loss rate	5%	
Atmospheric correction	10%	
Missing energy correction	5%	the primary dependences
T O T A L	20%	quadratic sum of all

The simulation program uses 20 km for the attenuation length by the Mie scattering (L_M) at the ground level. The density of the scattering center decreases exponentially with the height with the scale height of H_M=1.2 km. Both generation and reconstruction use the same values of L_M and H_M. We studied the effect of the Mie scattering uncertainty by intentionally taking a different set of parameters for the generation and reconstruction of events. It is seen that event reconstruction with wrong understanding of the atmospheric transparency could lead to both larger systematic shift and poorer resolutions on the energy determination. On the other hand, the angular reconstruction had no influence of wrong atmospheric parameters because our method to determine event trajectories is decoupled from the procedure to reconstruct longitudinal shower profile (see § 3).

Although the systematic shift caused by reconstructions with the wrong parameters is not negligible, it should be remarked that the results suggest that 10% shift of average reconstructed energy is equivalent to $\Delta L_M = {}^{+6}_{-3}$ km, or $\Delta H_M = \pm$ 0.36 km where ΔL_M and ΔH_M are the errors of L_M and H_M. We believe this level of accuracy can be achieved by the laser calibration. The extinction by the Rayleigh scattering can be calculated reliably and its contribution to the systematic uncertainty is negligible compared with the Mie scattering. We estimate that the energy uncertainty arising from the atmospheric correction can be controlled at the level of 10%. The X_{max} was affected by the wrong atmospheric parameters by average shift of $\pm$5 g/cm^2.

The measurement of extremely high energy cosmic showers has no convenient way of calibrating the energy scale. However, the accuracy of the measurement can be estimated directly from the uncertainties of the numbers used for the energy calculation. The accuracies we intend to achieve in TA for these numbers are listed in Table VIII.

The major contributions are from the uncertainties of scintillation efficiency, calibration, atmospheric correction and overall shower correction each at the level of 5–10%. A quadratic sum of all factors in the table gives 20% and this is the accuracy of absolute energy we expect to achieve at TA.

The uncertainty of angle determination is dominated by the reconstruction error already taken into account in the simulation. The absolute alignment of PMT and telescope can be calibrated with an accuracy better than 0.1° by shooting the laser from the center of the station.

Table IX. Resolution and systematic accuracy of TA

Observable	(unit)	Resolution	Sys. Uncert.
Energy	(%)	6	20
Angle	(°)	0.8	0.1
X_{max}	(g/cm^2)	18	15

The simulation indicates that the value of X_{max} changes depending on which functional shape to be used for fitting the longitudinal profile near the shower maximum. This difference is approximately 15 g/cm^2. The discrepancy between the generated and the reconstructed X_{max} is comparable to this shift as illustrated in Fig. 34. We take 15 g/cm^2 as the systematic uncertainty of measuring the X_{max}. It should be noted that the different shower simulation programs predict different X_{max} for the particles with the same energy. For example, X_{max} is 827 g/cm^2 for 10^{20}eV proton by CORSIKA whereas AIRES predicts 863 g/cm^2. The ability of TA to discriminate primary cosmic ray particle mass will be significantly improved if the theoretical understanding of cascade shower improves and the prediction of the Monte Carlo becomes more reliable.

The resolution and systematic uncertainties of energy, angle and X$_{max}$ measurement is summarized in Table IX for 10^{20}eV protons.

4.3 Primary Photon Identification

Shower characteristics depend on primary energy and arrival direction because the Landau-Pomeranchuk-Migdal (LPM) effect[52)76)] and cascading in the geomagnetic field are affected by particle energy and geomagnetic field strength.

Figure 38 shows average X_{max} as a function of primary energy. Average X_{max} of γ-ray primary has been calculated with zenith angles of 54.0° and 61.6°(open circles and crosses,respectively) and the cases of south/north arrival directions. Ones of proton and iron primaries are also plotted with solid and broken lines in the same figure. Though average X_{max} of proton and iron showers are increasing with a constant rate(elongation rate), one of γ-ray shower has much larger elongation rate in comparison with hadronic showers and the rate becomes a larger because of the LPM effect. The geomagnetic cascading starts its contributions to air shower development above energies of several times 10^{19}eV which depends on the arrival direction of γ-ray. Then, average X_{max} is decreasing and reaches at the minimum values.

The X_{max} distributions for showers initiated by protons and γ-rays with energy of $10^{19.5}$, 10^{20} and $10^{20.5}$eV and zenith angle of 39.6°, 54.0° and 61.6° are shown in Fig. 39. All distributions here are shown as ones after taking into account a detector resolution to determine X_{max} of $\sim$ 30 g/cm^2. Typically, X_{max} distribution of

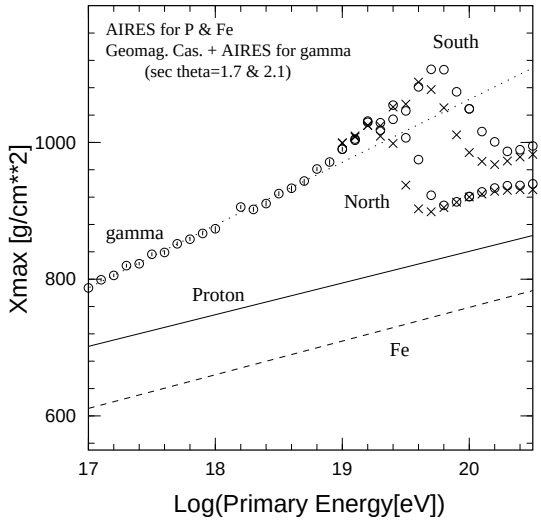

Fig. 38. Average X_{max} for showers initiated by proton, Fe and γ-ray as a function of primary energy. Proton and Fe showers were simulated with AIRES-QGSJET. X_{max} of γ-ray showers from south and north with zenith angles of 54.0° and 61.6° are shown.

γ-ray with energy of 10^{20}eV and zenith angle of 54.0° distributes broadly because LPM showers and showers with geomagnetic cascading effect are mixed together.

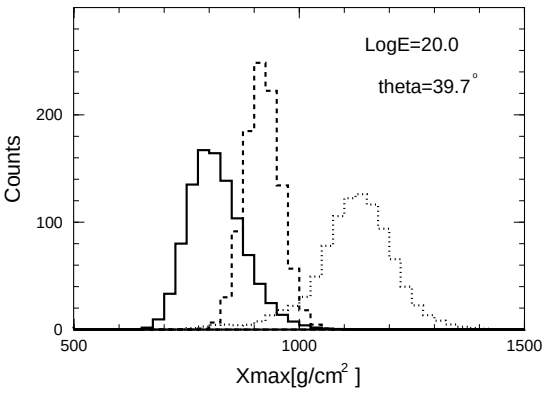

Fig. 39. X_{max} distributions for proton and gamma-ray showers with energy of 10^{20}eV. Zenith angle of 39.7° is assumed. X_{max} distributions of gamma-ray showers with arrival directions from south and north are shown in separately. All distributions here are shown as ones after taking into account a detector resolution for X_{max} of $\sim 30 g/cm^2$.

4.4 Neutrino Detection

4.4.1 Neutrino Production and Propagation

Here we describe the potential to detect neutrinos of energies more than 10^{16}eV through deeply penetrating air showers using TA. Assuming some simple conservative trigger and selection requirements with a monocular detection technique which uses each detector station for air showers in an independent way, we obtain the acceptance for deeply penetrating air showers as induced by high energy neutrinos by Monte Carlo method. We then give the expected event rates for two neutrino fluxes as predicted in different proton AGN models.

The recent discovery of near-maximal ν_e-ν_μ and ν_μ-ν_τ mixing[60] has a significant impact on the detection strategy. The proposed astrophysical sources produce predominantly ν_μ with very small admixtures of ν_τ. However, these sources are so far away that, even at the high energies of interest here, mixing is complete by the time they reach the Earth. We therefore assume a $\nu_e : \nu_\mu : \nu_\tau$ ratio of 1 : 1 : 1 at the Earth's surface.

4.4.2 Downward Neutrinos

Neutrinos produce showers in most interactions with the atmosphere which are of different nature depending on the process in consideration. We consider both inelastic charged and neutral current interactions which always produce hadronic showers. In the case of charged current electron neutrino interactions the emerging electron contributes in addition a pure electromagnetic shower carrying a large fraction of the incoming particle energy.

For a neutrino flux dI_ν/dE_ν interacting through a process with differential cross section $d\sigma/dy$, where y is the fraction of the incident particle energy transferred to the target, the event rate for deeply penetrating showers can be obtained by a simple convolution:

$$Rate[E_{sh} > E_{th}] = N_A \rho_{air} \int_{E_{th}}^{\infty} dE_{sh} \int_0^1 dy \frac{dI_\nu}{dE_\nu}(E_\nu) \frac{d\sigma}{dy}(E_\nu, y) \epsilon(E_{sh}) \quad (4.2)$$

where N_A is Avogadro's number and ρ_{air} is the air density. The energy integral corresponds to the shower energy E_{sh} which is related to the primary neutrino energy E_ν in a different way depending on the interaction being considered. ϵ is a detector acceptance, a function of shower energy, which corresponds to the volume and solid angle integrals for different shower positions and orientations with respect to the detector. The function is different for showers induced by charged current electron neutrino interactions from those arising in neutral current or muon neutrino interactions. This is because hadronic and electromagnetic showers have differences in the particle distributions functions, particularly for muons. For $(\nu_e + \overline{\nu}_e)N$ charged current interactions, we take the shower energy to be the sum of hadronic and electromagnetic energies, $E_{sh} = E_\nu$. For $(\nu_\mu + \overline{\nu}_\mu)N$ charged current interactions and for neutral current interactions, we take the shower energy to be the hadronic energy, $E_{sh} = yE_\nu$. In the case of ν_τ, we also take into account the decay length of secondary τ, subsequent decay of τ, and another energy deposit into air shower induced by decayed electrons, photons, and hadrons. The τ decay length is often long enough and two subsequent energy depositions into air showers can be seen with in the detector FOV.[77] We use the inelasity y as a function of E_ν from a reference,[61] while $< y > \sim 0.25$ does not de-

pend strongly on the primary energy beyond 10^{16}eV in both cases of charged and neutral current interactions. Assuming optimized efficiency for triggering on nearby as well as distant events and neglecting angular factor and Mie scattering attenuation, an estimate of signal to noise generated in a time during which the track is in view of a PMT is given by:

$$\frac{S}{N} = \frac{N_e N_\gamma}{4\pi} \left(\frac{c}{B}\right)^{1/2} \frac{e^{-r/\lambda_R}}{R_P^{3/2}} \left(\frac{\epsilon D^3}{d}\right)^{1/2} ,$$

where N_e is the number of electrons in the air shower generating the light, N_γ is the fluorescent yield which is measured to be $\sim$5 photons/electron/m, B is the night sky background at new moon phase, which is measured to be $\sim 2 \times 10^5$ photons m^{-2} sr^{-1} μs^{-1} over the wave length range 310–440 nm including atmospheric airglow, $R_P$is the impact parameter, λ_R is the Rayleigh scattering length ($\sim$ 18 km), ϵ is the overall optical efficiency for converting photons into photoelectrons, d and D are the diameters of the PMT and mirror aperture respectively. Next, we convert electron size N_e to energy in order to obtain an estimate for energy triggering thresholds. We take:[62]

$$E = 1.6 \times 10^{-9} N_e \quad ,$$

where E is the primary energy in EeV. Also assuming $r = R_P$, $\epsilon = 0.2$, $d = 0.06$m, and $D = 3$m, a crude estimate of the energy threshold is given by:

$$E_{th}[\mathrm{EeV}] = 10^{-4} \left(\frac{S}{N}\right) R_P^{3/2} e^{R_P/\lambda_R} \quad ,$$

where R_P is in km. E_{th} as a function of R_P in cases of $S/N = 2$ and 4 is shown in Fig. 40. This simple estimate suggests that the sensitive TA detector optics and readout devices should allow us the lower detectable energy threshold of 10^{16}eV and the more statistics for AGN neutrino events because of the steep slope of the flux spectrum shown in the previous section. This is a good advantage of the TA detector. Furthermore realistic acceptance estimates from Monte Carlo simulation study for neutrinos as a function of the primary energy will be described just later.

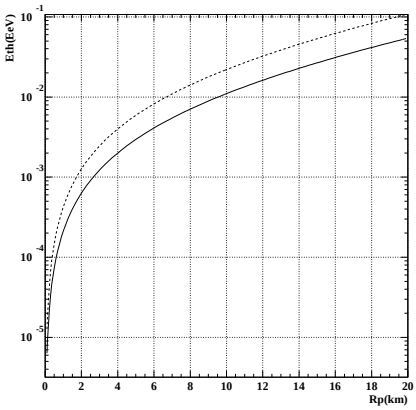

Fig. 40. A simple estimate of the minimum detectable energy in EeV as a function of impact parameter R_P in km in cases of PMT trigger levels $S/N = 2$ and 4.

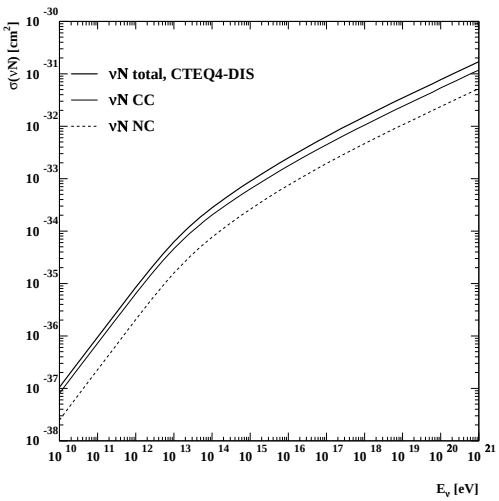

Fig. 41. Cross sections for interactions according to the CTEQ4-DIS parton distributions: dashed line $\sigma(\nu_l N \to \nu_l + anything)$; thin line, $\sigma(\nu_l N \to l^- + anything)$; thick line, total (charged-current plus neutral-current) cross section.

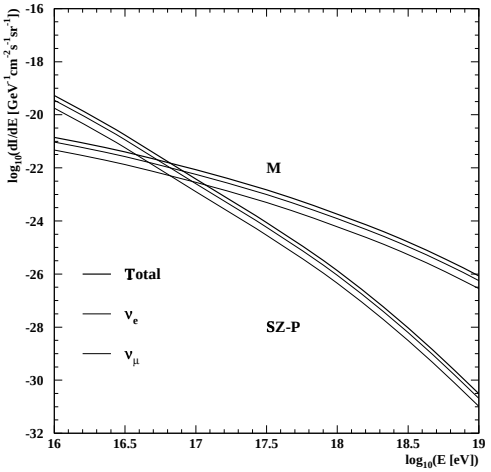

Fig. 42. Neutrino flux predictions in the EeV range as labeled in the text.

We use new calculations of the cross sections for charged-current and neutral current interactions of neutrinos with nucleons,[61,63] according to the CTEQ4-DIS (deep inelastic scattering) parton distributions.[64] The CTEQ4-DIS parton distributions take account of new information about the parton distributions within the

nucleon[65] using more accurate and extensive DIS data than before from New Muon Collaboration (NMC)[66] and DESY ep collider HERA,[67,68] as well as new data from E665.[69] The cross section for the charged-current reaction $\nu_l N \to l^- + anything$ as a function of the neutrino energy E_ν is shown in Fig. 41 (thin solid line). At low energies the charged-current cross section σ_{CC} rises linearly with E_ν. For energies exceeding about 10^4 GeV, the cross section is damped by the W-boson propagator. Also Fig. 41 shows the neutral-current cross section σ_{NC} for the reaction $\nu_l N \to \nu_l + anything$ (dashed line), together with σ_{tot}, the sum of charged-current and neutral-current cross sections (thick solid line). Since the valence contribution is negligible for $E_\nu > 10^6$ GeV, νN and $\overline{\nu} N$ cross sections become equal.

Here we select two typical models for neutrino production in AGN as shown in Fig. 42. First model assumes shock acceleration in the AGN cores and predicts relatively flat fluxes up to energies of about 10^{15}eV. For our event rate calculation we select the prediction of,[70] labeled SZ-P. There is however recent evidence that the GeV to TeV gamma ray emission observed from AGN corresponds to the blazar class. Most recent models for the proton blazars site the acceleration in the jets themselves. We use the prediction of,[18] labeled M, which illustrates that the emitted neutrinos may extend well into the EeV region.

Each simulation for a given primary cosmic ray (electron neutrino, muon neutrino, tau neutrinos, or proton) was performed at fixed energy. The shower energy of neutrinos depends on the generation as described above. For each shower energy, the mean depth of proton shower maximum was determined from simulations.[71] For each primary particle at each energy, the mean of the interaction length $X_1$was determined from the above interaction cross sections of neutrinos with nucleons or that of protons, $83.1(E/\mathrm{GeV})^{-0.052}$ g/cm^2.[72] The shower energy determines the shower size at maximum, N_{max}.[27] Given N_{max}, X_{max}, and X_1, the complete longitudinal profile was described by the Gaisser-Hillas function.[62] The NKG lateral distribution function[73,74] normalized with the Gaisser parameterization has been used for the total number of electrons and positrons in hadronic (electromagnetic) cascade showers to determine the location where fluorescence lights are produced. We took into account the fluctuations of the first interaction depth, impact point, and directional angles of air shower cores with appropriate distributions but not air shower size fluctuations.

The light yield arriving at the detector site is calculated. Rayleigh and Mie scattering processes are simulated, with full account taken of the spectral characteristics of the light. The isotropically emitted fluorescence light, as well as direct and scattered Cherenkov light, is propagated. Night sky background noise is added to the signal. All processes that affect to overall optical efficiency; mirror area and reflectivity, optical filter transmission, PMT quantum efficiency factors are folded with the light spectrum to give the photoelectron yield in each PMT, due to signal and noise.

A "fired" PMT is defined to require that its instantaneous photoelectron current is greater than the 4σ noise level of the night sky background. We preselected events if at least one of 10 eyes contains at least 6 firing PMTs. To ensure track quality, we cut events of which shower maximums are not viewed by any eye. Finally to reject proton background events, we selected only events with $X_{max} > 1700$ g/cm^2. We obtained the detector aperture corresponding the above selection cuts and calculated them into the acceptances multiplying the appropriate interaction length of neutrino with nucleon. The results are shown in Fig. 43 for both electron and muon neutrinos as a function of the primary energy. We have estimated event rates for several energy threshold and selection cuts using a variety of models for the neutrino fluxes from proton AGN models which assume the proton acceleration region is at the core or the jets[70].[18] The origins of the highest energy cosmic rays are not well understood, but cosmic rays should be accompanied by very high energy neutrinos in all models. The absolute normalization and energy dependence of the fluxes depends largely on production models. The TA detector as a neutrino telescope ultimately will probe extraterrestrial accelerator sources using enough statistics of AGN neutrino events. Also we can distinguish between the assumptions for the location in AGN where protons could be accelerated well from the observed neutrino spectrum

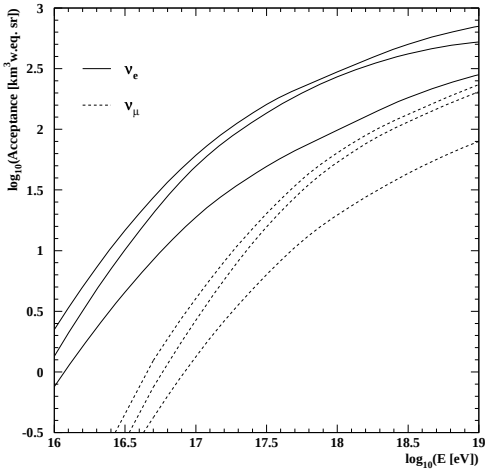

Fig. 43. Acceptance of the TA detector to neutrino induced air shower. Volume units are km^3 of water equivalent. The higher, middle, and lower curves corresponds to events after preselection, track quality, and proton rejection cuts.

Table X. Annual event rates in the TA detector for neutrino induced air showers with fluxes from the AGN-jet model[18] (see text). The duty factor of 10% was assumed.

CC ν_e	CC ν_μ	CC ν_τ	NC	Total
9.2	2.4	8.5	7.2	27.3

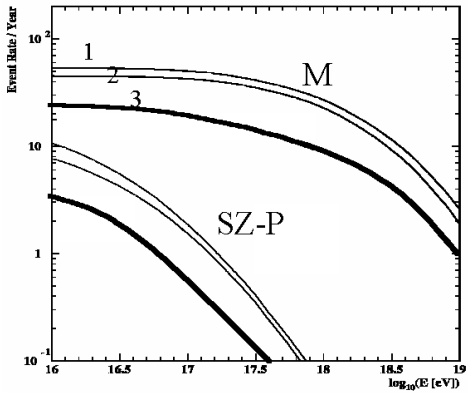

Fig. 44. Annual event rates as a function of the lower threshold energy with the TA detector for neutrino induced air showers. Neutrino fluxes from two different AGN models (see text) are assumed Three kinds of curves from each proton AGN model correspond to the required selections.

Table XI. Expected number of ν_τ-induced electromagnetic showers detected by atmospheric fluorescence only with one detector station of TA. The assumed sources are noted and one year of running with duty cycle of 6 % is assumed.

Greisen	AGN-jet	Topological Defect	Z-burst
9.8	220	72	12

once we can detect neutrinos well with $E_\nu > 10^{16}$eV.

4.4.3 Earth-skimming Neutrinos

Charged current neutrino interactions near the earth's surface produce leptons that emerge from the Earth. However, electrons lose their energy quickly in the Earth and so typically do not emerge to be detected by fluorescence. Here we concentrate on the signal from τ decays, which produce electromagnetic showers that point to the horizon. The tau decay length is:

$$L_\tau = c\tau_\tau \frac{E_\tau}{m_\tau} \approx 4.9\ km \frac{E_\tau}{10^{17}\ eV} \quad . \qquad (4.3)$$

Electrons and neutral pions are often among the tau decay products. We assume that tau decays initiate electromagnetic showers with probability roughly 80 % and typical energy about $E_\tau/3$. Event rates were calculated for the four neutrino sources given in Fig. 2.[16] The total annual rates for these sources are listed in Table 4.4.3 assuming the duty cycle of 10%. Also Fig. 4.4.3 shows the annual rates as a function of the threshold energy of neutrino.

§5. Summary

- AGASA has made it clear that super-GZK puzzle is substantial.
- The solution candidates are expected to come from fundamental particle physics like super heavy particle produced at the GUT era, from unknown astronomical objects like AGN-jet proton acceleration, or from unknown physics process like the breakdown of relativity.
- In order to solve this puzzle, a new cosmic ray detector with powerful particle identification as well as a huge detection aperture is indispensable.
- TA can observe about 60 times larger amount of cosmic ray events than AGASA and descriminate among gamma, proton, and heavy composition like iron as the dominant primary particle species by measuring longitudinal shower development in a huge atmospheric volume as an active target and absober fully utilizing the advanced air fluorescence technique.
- It also allows us to open the new window of extremely high energy neutrino astronomy mainly by clear separation of the primary neutrino as deeply penetrating air shower event against proton contamination.
- The performance of the TA detector is well estimated by Monte Carlo study;
  - energy resolution of 20% taking into account systematic error dominantly from atmospheric extinction estimate,
  - pointing accuracy of 0.6deg with stereo reconstruction for higher energy events and 1.2-1.5deg with monocular one for lower energy events,
  - X_{max} resolution of 25 g/cm^2 with stereo reconstruction enough to examine the discrepancy of roughly 100 g/cm^2 on average between the average X_{max} from gamma-induced air shower and that from proton induced one.
- Its R&D items have proceeded very well. The ad-

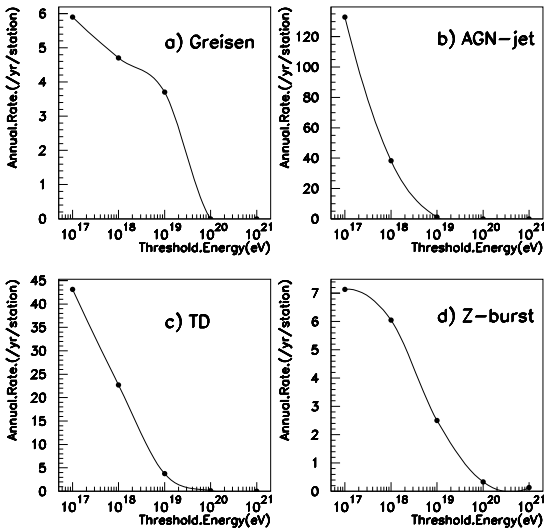

Fig. 45. Expected annual rate as a function of the threshold energy of neutrinos for ν_τ-induced electromagnetic showers detected by atmospheric fluorescence only with one TA station. The assumed sources are a) Greisen process, b) AGN-jet, c) Topological Defect, d) Z-burst models. The duty cycle of 10% is assumed.

vanced techniques of frontend electronics, trigger, and atmospheric monitoring method have been already developed.

- Finally, the TA project has big potential to point out the super-GZK source in a clearly experimental way.

Acknowledgement

I am indebted to my colleagues in the Telescope Array Collaboration, especially those who have contributed text to the Telescope Array Design Report, for assistance in the preparation of this report. I would like to special acknowledge the contributions of Y. Arai, H. Inoue, Y. Tanaka, M. Kobayashi, M. Fukushima, M. Teshima, S. Yoshida, S. Ogio, N. Inoue, T. Yamamoto, M. Takeda, P. Sokolsky, G. Tompson, K. Martens, and L. Wiencke. This work has been supported in part by the Ministry of Education, Science, and Technology.

1) M. Takeda et al.: Phys. Rev. Lett. **81** (1998) 1163.
2) J.D. Bird et al.: Phys. Rev. Lett. **71** (1993) 3401.
3) B.N. Afanasiev et al.: Proc. 24th ICRC, Roma, **2** (1995) 756.
4) K. Greisen: Phys. Rev. Lett. **16** (1966) 748.
5) S. Yoshida and M. Teshima, Prog. Theor. Phys. **89**, 833 (1993).
6) G.T. Zatsepin and V.A. Kuzmin: JETP Letters **4** (1966) 78.
7) E. Waxman: Phys. Rev. Lett. **75** (1995) 386.
8) C.T. Hill, D.N. Schramm and T.P. Walker: Phys. Rev. **D36** (1987) 1007.
9) P. Bhattacharjee, C.T. Hill and D.N. Schramm: Phys. Rev. Lett. **69** (1992) 567.
10) T. J. Weiler, Astropart. Phys. **11**, 303 (1999).
11) D. Fargion, B. Mele, and A. Salis, Astrophys. J. **517**, 725 (1999).
12) S. Coleman and S.L. Glashaw: Phys. Rev. **D59** (1999) 116008.
13) J. Alvarez-Muniz and F. Halzen: astro-ph/0102106.
14) K.S. Capelle, J.W. Cronin, G. Parente and E. Zas: Astropart. Phys. **8** (1998) 321.
15) M. Sasaki: Proc. the 1st workshop on *Neutrino Oscillations and their Origin*, (2000) 79.
16) J.L. Feng, P. Fisher, F. Wilczek, and T.M. Yu: hep-ph/0105067; MIT-CTP-3122; MIT-LNS-01-294.
17) F.W. Stecker: Astrphys. J. **228** (1979) 919.
18) K. Mannheim: Astropart. Phys. **3** (1995) 295.
19) G. Sigl, et al.: Phys. Rev. **D59** (1999) 043504.
20) S. Yoshida, G. Sigl and S. Lee: Phys. Rev. Lett. **81** (1998) 5505.
21) M. Sasaki et al.: Proc. 25th ICRC, **5**, 369 (Durban, 1997).
22) The Telescope Array Project: Design Report. July 2000. http://www-ta.icrr.u-tokyo.ac.jp
23) M. Kobayashi *et al.*, Nucl. Inst. Meth. A **337**, 355 (1992).
24) M. V. Korzhik *et al.*, Nucl. Inst. Meth. B **B72**, 499 (1992).
25) S. Baccaro *et al.*, Nucl. Inst. Meth. A **361**, 209 (1995).
26) N. Tsuchida *et al.*, Nucl. Inst. Meth. A **385**, 290 (1997). KEK preprint 99-22, June 1999.
27) R. M. Baltrusaitis et al.: Phys. Rev. D **31**, 2192 (1985).
28) J. Boyer et al.: Proc. 24th ICRC, **3**, 429 (Rome, 1995).
29) M. Sasaki et al.: Proc. 27th ICRC, **HE7.1** (Hamburg, 2001).
30) M. Takeda *et al.*, 26th ICRC, Salt Lake City, OG 4.5.16 (1999).
31) R.T.H. Collis, Q.J.R. Meteorol. Soc. **92**, 220 (1966).
32) W. Viezee, E.E. Uthe, and R.T.H. Collis, J. Appl. Meteorol. **8**, 274 (1969).
33) H.R. Pruppacher and J.D.Klett, *Microphysics of Clouds and Precipitation* (Reidel, Dordrecht, Holland, 1978), pp.20-21.
34) T. Okita, J.Meteorol. Coc. Jpn. **40**, 39 (1962).
35) R.T. Brown, Jr.,J. Appl. Meteorol. **12**, 698 (1973).
36) W. Viezee, J. Oblanas, and R.T.H. Collis, AFCRL-TR-73-0708, Air Force Cambridge Research Laboratories, Bedford, Mass. (1973), NTIS 776054.
37) R.H. Kohl, J. Appl. Meteorol. **17**, 1034 (1978). R.H. Kohl, J. Appl. Meteorol. **18**, 712 (1979).
38) R.T. Brown, Jr., J. Appl. Meteorol. **18**, 711 (1979).
39) J.A. Curcio and G.L. Knestrick, J. Opt. Soc. Am. **48**, 686 (1958).
40) R.W. Fenn, Appl. Opt. **5** 293 (1966).
41) O.D. Barteneva, Bull. Acad. Sci. USSR No. 12, 1, 852 (1960).
42) S. Twomey and H.B. Howell, Appl. Opt. **4**, 501 (1965).
43) J.D. Klett, Appl. Opt. **20**, 211 (1981).
44) F.G. Fernald, B.M. Herman, and J.A. Reagan, J. Appl. Meteorol. **11** 482 (1972).
45) F.G. Fernald, Appl. Opt. **23**, 652 (1984).
46) A. Ansmann, U. Wandinger, M. Riebesell, C. Weitkamp, and W.W. Michaelis, Appl. Opt. **31**, 7113 (1992).
47) RM. Sasaki, TA-Note-97-001 (1997).
48) S. J. Sciutto, GAP97-029 (1997).
49) R. Ghandi, C. Quigg, M. H. Reno, and I. Sarcevic, Astropart. Phys. **5**, 81 (1996); Phys. Rev. D **58**, 093009 (1998).
50) B. L. Emerson, Ph.D Thesis, University of Utah (unpublished) (1992).
51) S. Yoshida, G. Sigl, and S. Lee, Phys. Rev. Lett. **81**, 5505 (1998).
52) L. D. Landau and I. J. Pomeranchuk, Dokl. Akad. Nauk. SSSR **92**, 535 (1953).
53) A. B. Migdal, Phys. Rev. **103**, 1811 (1956).
54) B. McBreen and C. J. Lambert, Phys. Rev. D **24**, 2536 (1981).
55) T. Stanev, and H. P. Vankov, Phys. Rev. D **55**, 1365 (1997).
56) S. J. Sciutto, GAP97-029 (1997).
57) T. Erber, Rev. Mod. Phys. **38**, 626 (1966).
58) V. H. Bayer, B. M. Katkov, and V. S. Fadin, in *Radiation of relativistic electrons* (Moscow, Atomizdat, 1973).
59) V. Anguelov and H. Vankov. *No Identification*
60) S. Fukuda et al (Super-Kamiokande Collaboration), Phys. Rev. Lett. **86** (2001) 5656-5660.
61) R. Gandihi, C. Quigg, M. H. Reno, and I. Sarcevic, Astropart. Phys. **5** 81 (1995).
62) T. K. Gaisser and A. M. Hillas, in *Proceedings of the 15th International Cosmic Ray Conference, Plovdiv, Bulgaria, 1977*, Vol. 7, p. 353.
63) R. Gandihi, C. Quigg, M. H. Reno, and I. Sarcevic, Phys. Rev. D **58**, 093009 (1998).
64) CTEQ Collaboration, H. L. Lai *et al.*, Phys. Rev. D **55** 1280 (1997).
65) C. Quigg, "Neutrino Interaction Cross Sections", FERMILAB-CONF-97/158-T.
66) NMC, M. Arneodo *et al.*, Phys. Lett. B **36** 471 (1995).
67) H1 Collaboration, S. Aid *et al.*, Nucl. Phys. B **439** 471 (1995); Nucl. Phys. B **470** 3 (1996).
68) ZEUS Collboration, M. Derrick *et al.*, Z. Phys. C **65** 379 (1995).
69) E665 Collaboration, M. R. Adams *et al.*, Phys. Rev. D **54**, 3006 (1996).
70) A. P. Szabo and R. J. Protheroe, Proc. High Energy Neutrino Astrophysics Workshop (U.Hawaii, March 1992), ed. V.J.Stenger, J.L.Learned, S.Pakvasa, and X.Tata, World Scienctific, 1993, p24.
71) T. K. Gaisser *et al.*, Phys. Rev. D **47**, 1919 (1993).
72) M. Honda *et al.*, Phys. Rev. Lett., **70**, 525 (1993).
73) K. Kamata and J. Nishimura, Prog. Theor. Phys. Suppl. **6**, 93 (1958).
74) K. Greisen, Prog. Cosmic Ray Physics **3**, 1 (1956).
75) F. Kakimoto *et al.*, Nuclear Instruments and Methods, A **373**, 572 (1996). bitemLandau L. D. Landau and I. J. Pomeranchuk, Dokl. Akad. Nauk. SSSR **92**, 535 (1953).
76) A. B. Migdal, Phys. Rev. **103**, 1811 (1956).
77) J.G. Learned and S. Pakvasa, Astropart. Phys. **3**, 267 (1994).